Doctorate Dissertation (Censored)
博士論文（要約）

Study of J/ψ production in 12 GeV proton-nucleus collisions

(12 GeV陽子原子核衝突による
J/ψ粒子生成の研究)

A Dissertation Submitted for Degree of Doctor of Science
September 2018
平成30年9月　博士（理学）申請

Department of Physics, Graduate School of Science,
The University of Tokyo
東京大学大学院理学系研究科物理学専攻

Koki Kanno
菅野　光樹

Abstract

Study of the J/ψ production at low energy provides critical information on nonperturbative processes of charm quark production. The production cross section of the J/ψ in 12 GeV $p + \mathrm{C}$ and $p + \mathrm{Cu}$ reactions has been measured using invariant mass spectra of e^+e^- pairs. The center of mass energy is 5.1 GeV, which is the lowest energy in the former experiments for the J/ψ production by hadron interactions and is just above the threshold of the simplest final state, ppJ/ψ. Effects of nonperturbative J/ψ production is expected to appear near the threshold. The experiment has been conducted as KEK-PS E325 experiment in EP1-B beamline at KEK. The total production cross sections of the J/ψ mesons are found to be $7.0\ ^{+3.4}_{-3.1}$(stat.) $^{+2.9}_{-2.6}$ (syst.) nb and $3.8\ ^{+9.5}_{-3.8}$(stat.) $^{+2.8}_{-3.8}$ (syst.) nb for the carbon target and for the copper target, respectively. The 95% confidence level upper limits are 21 nb and 33 nb for the carbon target and for the copper target, respectively. The result for the carbon target shows a slight excess from the contribution of conventional hard processes to the J/ψ production, while the result for the copper target shows no excess. The contribution of conventional hard processes is evaluated with a theoretical calculation which reproduces results of former experiments. This excess is examined in terms of intrinsic charm which is a nonperturbative charm component in a nucleon and is not taken into account in that theoretical calculation. The probability of intrinsic charm in a nucleon is found to be $0.09 \pm 0.06\%$ in the present study, which is consistent with the results of recent global QCD analyses. This contribution of intrinsic charm to the J/ψ production is also not inconsistent with the J/ψ cross sections obtained in former experiments in pp collisions. The ratio of the cross section for the carbon target to that for the copper target, which represents the mass number dependence, is found to be $1.0\ ^{+2.8}_{-0.7}$ in the present study. This ratio is consistent with the ratio of intrinsic charm contribution, even considering the possible absorption of the J/ψ by the nuclear matter. Due to a large experimental uncertainty, the production cross section of the J/ψ in the present study is consistent with the intrinsic charm scenario and the conventional scenario that the J/ψ production is only originated from hard processes.

Contents

Chapter 1

Introduction

1.1 Overview

In November 1974, two independent groups at Stanford Linear Accelerator Center and Brookhaven National Laboratory almost simultaneously have discovered the J/ψ meson [1, 2], a flavor-neutral bound state consisting of a charm quark and a charm antiquark. The production mechanism of a charmonium, a bound state of a charm quark and a charm antiquark, have widely been studied after the discovery of the J/ψ, because their production includes both perturbative and nonperturbative aspects of quantum chromodynamics (QCD), the theory of the strong interaction between quarks and gluons. The charm quark mass $m_c \sim 1.3$ GeV/c^2 [3] is much larger than the QCD scale $\Lambda_{\rm QCD} \sim 0.3$ GeV [4], thus one might expect that it is possible to evaluate quantitatively the rate for the production of a $c\bar{c}$ pair with a perturbative QCD theory. On the other hand, the evolution of a $c\bar{c}$ pair into a physical state of a charmonium involves nonperturbative effects.

So far, the production cross section of the J/ψ by the hadron interactions has been measured in the wide center of mass energy range, $\sqrt{s} = 6.7$ GeV to 13 TeV. However, no measurements for the J/ψ production by hadron interactions at low energy near the production threshold have been carried out yet. Nonperturbative contributions to the J/ψ production are expected to become prominent at lower energy than the former experiments. Intrinsic charm in a nucleon is one of the examples, whose existence has not been established. Intrinsic charm is a five particle Fock state component of a nucleon which includes a $c\bar{c}$ pair. In pA collisions, for example, this $c\bar{c}$ pair in a proton can be liberated by a collision of the proton and a target nucleus and can be evolved into a physical state of the J/ψ.

This thesis is dedicated to the analysis of the production cross section of the J/ψ meson in 12 GeV pA reactions, corresponding to the center of mass energy $\sqrt{s} = 5.1$ GeV. This is the lowest energy experiment for the J/ψ production by

hadron interactions in all the experiments ever conducted. Actually, $\sqrt{s} = 5.1$ GeV is just above the threshold of the simplest final state ppJ/ψ, which is 4.97 GeV. Therefore one expects that the results of this study can provide crucial information on contributions of nonperturbative processes to the J/ψ production by hadron interactions.

The data for this analysis has been obtained at High Energy Accelerator Research Organization (KEK) 12 GeV Proton-Synchrotron (PS) in 2001 and 2002 by the KEK-PS E325 experiment, which has measured the dielectron mass spectra.

My major contributions as a KEK-PS E325 collaborator are energy calibration of the electromagnetic calorimeters, development of an event generator for the J/ψ, and the whole analysis on the production cross section of the J/ψ.

1.2 J/ψ production mechanism

In this section, production mechanism of the J/ψ is briefly described. The production of the J/ψ can be factorized into two components. The first component expresses the production of a pair of a charm quark and a charm antiquark. The charm quark mass $m_c \sim 1.3$ GeV/c^2 [3] is much larger than the QCD scale $\Lambda_{\rm QCD} \sim 0.3$ GeV [4], thus one might expect that it is possible to evaluate quantitatively the rate for the production of a $c\bar{c}$ pair with a perturbative QCD theory. The second component expresses the evolution of a $c\bar{c}$ pair into a physical state of the J/ψ. This evolution involves long distance scales at the order of $1/(m_c v)$, where v is the typical velocity of the charm quark in the charmonium bound state in the center-of-mass frame. The typical velocity for a charmonium is v^2 =0.25–0.3 [5]. The two components are separated in terms of their scales ($1/m_c \ll 1/(m_c v)$), and thus this two components can be factorized. This assumption is widely made in the majority of theories to describe the charmonium production. In this section, three prevalent theories, color single model (CSM), color evaporation model, and non-relativistic QCD (NRQCD) are briefly described.

1.2.1 Color singlet model

In color singlet model (CSM), a $c\bar{c}$ pair that evolves into a charmonium is required to have the same quantum number of the charmonium to be formed [6]. Thus, the quantum number of $c\bar{c}$ pair must be $^{2S+1}L_J = {}^3S_1$ and color singlet state for the J/ψ production. At leading order (LO) in α_s and at leading twist, the processes of

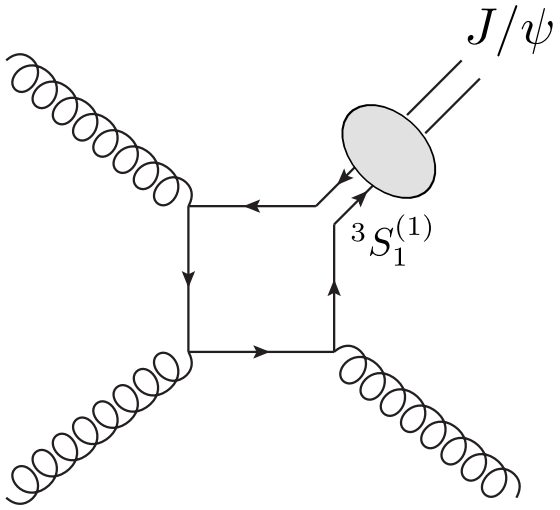

Figure 1.1: Example of the lowest order diagram for the direct J/ψ production through gluon fusion in the CSM. This diagram and diagrams shown later in this thesis are written with "JaxoDraw" [8].

the color singlet $c\bar{c}$ production are

$$\begin{aligned} gg &\to {}^1S_0, {}^3P_{0,\,2}, \\ gg &\to {}^3S_1 + g, {}^3P_J + g, \\ gq &\to {}^3P_J + q, \\ q\bar{q} &\to {}^3P_J + g. \end{aligned} \tag{1.1}$$

As for the J/ψ production, there is the contribution of the decay of the higher excited states (${}^3P_J \to {}^3S_1 + \gamma$) in the J/ψ production. It should be noted that the process $gg \to {}^3P_1$ is forbidden due to the on-shell gluons [7]. Figure 1.1 shows the lowest order diagram of the J/ψ production in the CSM. The CSM successfully predicted the production cross section of the charmonia at low energy [6]. However, it underestimated the Tevatron data in $p\bar{p}$ collisions at $\sqrt{s} = 1.8$ TeV by more than a order of magnitude [9]. Recently, the very large corrections to the CSM were found at next-to-leading order (NLO) and next-to-next-leading order (NNLO) in α_s [10]. It is not sure that the perturbative expansion in α_s converges. Furthermore, the CSM includes known infrared divergences in P-wave states, χ_c, production and decay processes.

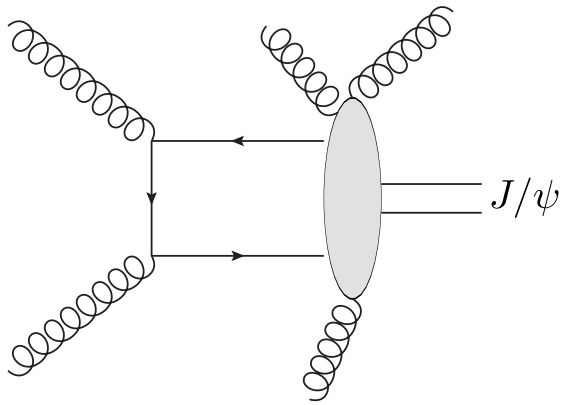

Figure 1.2: Example of the lowest order diagram for the direct J/ψ production through gluon fusion in the CEM.

1.2.2 Color evaporation model

In color evaporation model (CEM) [11, 12, 13, 14], the production cross section of a certain charmonium state H is expressed as some fraction f_H of the total production cross section of a $c\bar{c}$ pair with the invariant mass of less than $2m_D$, where m_D is the mass of the D meson which is the lightest meson containing a charm quark or a charm antiquark. A produced $c\bar{c}$ pair neutralize its color and make a bound state by interaction with a collision-induced color field, therefore it is called "color evaporation". Figure 1.2 shows a diagram for the J/ψ production with multiple gluon emissions. The probability that a $c\bar{c}$ pair evolves into a certain charmonium is assumed to be independent of the production energy, kinematic region, and process. Thus, the fraction f_H is determined by data. The CEM is consistent with the data in terms of the energy dependence of the J/ψ production cross section by hadron interactions in the center of mass energy $\sqrt{s}$ less than 60 GeV [15].

1.2.3 Non-relativistic QCD

Non-relativistic QCD (NRQCD) is an effective theory where quarks and antiquarks are treated non-relativistically [16, 17, 18]. The NRQCD itself is not a model and reproduces dynamics of full QCD at scale of order $m_Q v$ and smaller where m_Q represents the mass of the heavy quark Q, for example charm quark, and v represents the typical velocity of heavy quark Q in the bound state in the center-of-mass frame. In the NRQCD, the direct production cross section of a certain charmonium H is expressed as a sum of the products of a short-distance coefficient and a long-distance

NRQCD matrix element over possible quantum states of a $Q\bar{Q}$ pair,

$$\sigma_H = \sum_n \sigma_n(\Lambda) \langle \mathscr{O}_n^H(\Lambda) \rangle \tag{1.2}$$

Here Λ is the ultraviolet cutoff of the effective theory. The short-distance coefficient $\sigma_n(\Lambda)$ is the process-dependent partonic cross section for producing a $Q\bar{Q}$ pair with the given quantum state n and can be calculated perturbatively. The long-distance NRQCD matrix element $\langle \mathscr{O}_n^H(\Lambda) \rangle$ represents the hadronization of a produced $Q\bar{Q}$ pair into an observable state H. The index of the summation, n, denotes a given color, spin, and angular momentum state. The contribution of the color octet $c\bar{c}$ state to the charmonium production is taken into account with this summation as well as the color singlet contribution, whereas the CSM does not include the color octet contribution. In principal, there are infinite number of nonperturbative NRQCD matrix elements that must be summed over. However, the NRQCD matrix elements can be classified in terms of powers of the heavy quark velocity v, and be truncated at a given order of v. The NRQCD is a double expansion in terms of α_s and v. At LO in α_s and up to NLO in the velocity expansion, the process of the J/ψ production through the color octet $c\bar{c}$ states are

$$\begin{aligned}
&gg \to c\bar{c}[^1S_0^{(8)}] \to J/\psi + g, \\
&gg \to c\bar{c}[^3P_J^{(8)}] \to J/\psi + g, \\
&q\bar{q} \to c\bar{c}[^3S_1^{(8)}] \to J/\psi + gg, \\
&q\bar{q} \to c\bar{c}[^3S_1^{(8)}] \to \chi_J + g \to J/\psi + \gamma + g.
\end{aligned} \tag{1.3}$$

Figure 1.3 shows the lowest order diagram of the J/ψ production by the color octet $c\bar{c}$ state. The NRQCD is consistent with the data in terms of the energy dependence of the J/ψ production cross section by hadron interactions in the center of mass energy $\sqrt{s}$ less than 60 GeV [5], as the CEM does.

1.3 Nuclear matter effects on the J/ψ production

In pA collisions, the production of the J/ψ is modified from pp collisions because of the nuclear matter effects of the target A. These nuclear matter effects play important roles in the J/ψ production at Fermi National Accelerator Laboratory (FNAL), Relativistic Heavy Ion Collider (RHIC), and The Super Proton Synchrotron (SPS). This section describes the following major nuclear matter effects on the J/ψ production in pA collisions at low energy:

Nuclear shadowing: Modification of the parton distribution function (PDF).

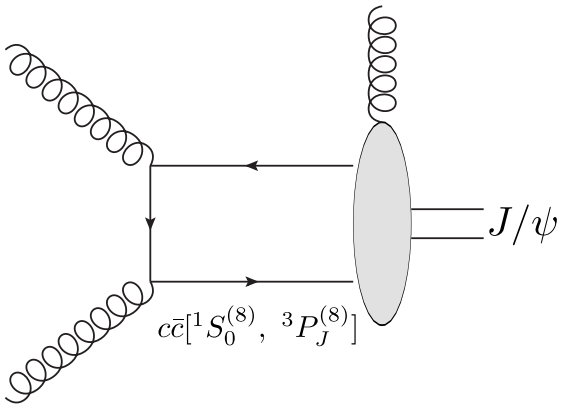

Figure 1.3: Example of the lowest order diagram for the direct J/ψ production through the color octet $c\bar{c}$ state generated by gluon fusion in the NRQCD.

Radiative energy loss: Modification of the momentum fraction of partons due to exchange or radiation of gluons with a target nucleus.

Absorption: Interaction of a pre-resonance $c\bar{c}$ state or a J/ψ meson with a target nucleus.

1.3.1 Nuclear shadowing

In a perturbative QCD theory, the production cross section for a hard process is generally assumed to be expressed as a product of PDFs and a hard scattering cross section of partons which can be calculated perturbatively. A PDF describes the probability density of quarks, antiquarks, and gluons in a free proton as a function of the fraction of the longitudinal momentum which a parton carries, x, and energy scale, Q^2. Since QCD itself does not predict the parton content of a proton, the shapes of the PDFs at the initial scale are determined by a fit to data taken mostly from deep inelastic scattering (DIS) and Drell-Yan (DY) dilepton production, using DGLAP evolution equation [19, 20, 21]. The DGLAP evolution equation describes the QCD evolution from the initial scale to a given energy scale.

Figure 1.4 shows an example of a PDF (CTEQ6.1M [22]) at the energy scale of $Q^2 = 9$ GeV^2 relevant to the J/ψ production. The peak structure around $x = 1/3$ for the up quark and the down quark is attributed to the valence quark component. In this PDF, the strange quark and the strange antiquark components are assumed to be identical for a given x, because the strange quark and antiquark generated from gluon splitting $g \to s\bar{s}$ and the asymmetry does not appear until at three loops in the perturbative QCD evolution [23]. This assumption is also applied to

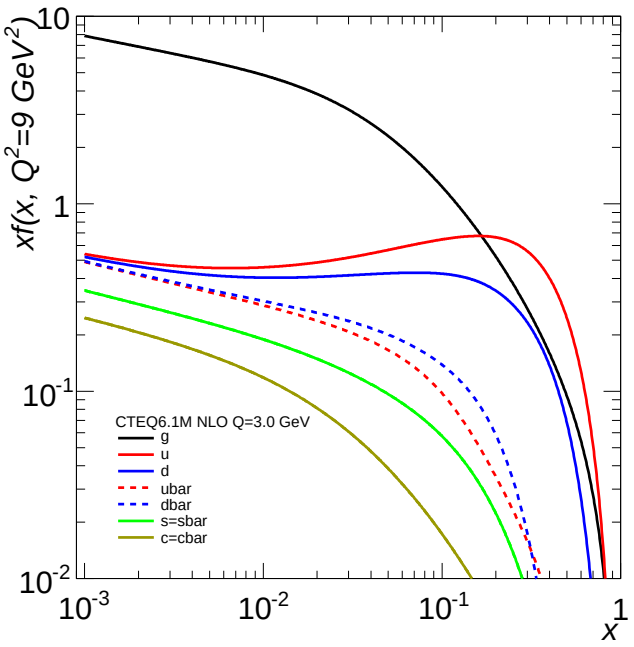

Figure 1.4: The PDF (CTEQ6.1M) for the quarks and the gluon at $Q = 9$ GeV^2.

the charm quark and the charm antiquark. Furthermore, the PDF for the charm quark and the charm antiquark is zero at the initial scale $\mu = 1.3$ GeV: $c(x, \mu) = \bar{c}(x, \mu) = 0$. This assumption is widely accepted for many models of PDFs. It should be noted that both the DIS experiments and DY dilepton production provide the direct information on only the quark and antiquark distributions, while they probe the gluon distribution indirectly. In general, there is a large uncertainty on the gluon distribution compared to the quark and antiquark distributions [24].

Through nuclear DIS experiments [25], the European Muon Collaboration (EMC) found that the PDFs for a proton bound in a nucleus were different from those for a free proton. Nuclear parton distribution functions (nPDF) has been developed for introducing the measured modification of the PDFs by the nuclear effect. The modification of the PDFs is typically introduced by the ratio

$$R_i^A(x, Q^2) = \frac{f_i^A(x, Q^2)}{f_i(x, Q^2)}, \tag{1.4}$$

where $f_i(x, Q^2)$ is a PDF of flavor i for a free proton and $f_i^A(x, Q^2)$ is a nPDF of flavor i for a proton bound in a nucleus A. The ratio shows a characteristic structure and the modification is classified into four regions as shown in Fig. 1.5. The regions are as follows:

Shadowing: In the low-x region ($x \lesssim 0.04$), the ratio shows $R_i^A(x, Q^2) < 1$, which means the number of partons for a proton bound in a nucleus decreases compared to a free proton. This phenomenon is believed to be caused by fusion of low-x gluons into a single high-x gluon due to the higher density of gluons in the nucleus than that in a free proton. It is should be noted that the overall modification of PDFs is often referred to as nuclear shadowing, while shadowing alone means the suppression of a PDF in low-x region.

Anti-shadowing: In the intermediate-x region ($0.04 \lesssim x \lesssim 0.4$), the ratio shows $R_i^A(x, Q^2) > 1$, which means the number of partons for a proton bound in a nucleus increases compared to a free proton. The fusion of low-x gluons into a single high-x gluon in shadowing region is believed to make an excess in this region.

EMC effect: In the higher-x region ($0.4 \lesssim x \lesssim 0.9$), the ratio shows $R_i^A(x, Q^2) < 1$ again.

Fermi motion: In the highest-x region ($0.9 \lesssim x$), the ratio shows $R_i^A(x, Q^2) > 1$ due to Fermi motion of a nucleon in a nucleus.

The origin of the modification in each region is still discussed [26, 27, 28].

The parametrization for nPDFs is usually based on the data taken from $l + A$ DIS experiments and DY dilepton production in pA collisions. Figure 1.5 shows an example of the ratio $R_i^A(x, Q^2)$ (EPS09 [29]) at the energy scale of $Q^2 = 9$ GeV^2 relevant to the J/ψ production. There is a large uncertainty in the gluon distribution compared to the valence quark and sea quark distributions. This is because the available data does not impose direct constraints on the gluon distribution as in the PDF of a free proton case.

1.3.2 Radiative energy loss

Radiative energy loss refers to the energy loss of a parton due to radiation or exchange of gluons with the medium. This phenomenon occurs as initial state energy loss and final state energy loss. Initial state energy loss occurs before a hard scattering of two partons, while final state energy loss occurs after that hard scattering. In initial state energy loss, an incoming parton radiates gluons when it traverses the medium. This leads to the decrease of momentum fraction x of the incoming parton, resulting in another modification to the PDF relative to pp collisions. In final state energy loss, an outgoing parton generated in a hard scattering radiates gluons when it traverses the medium. This also decreases the momentum fraction x of the outgoing parton.

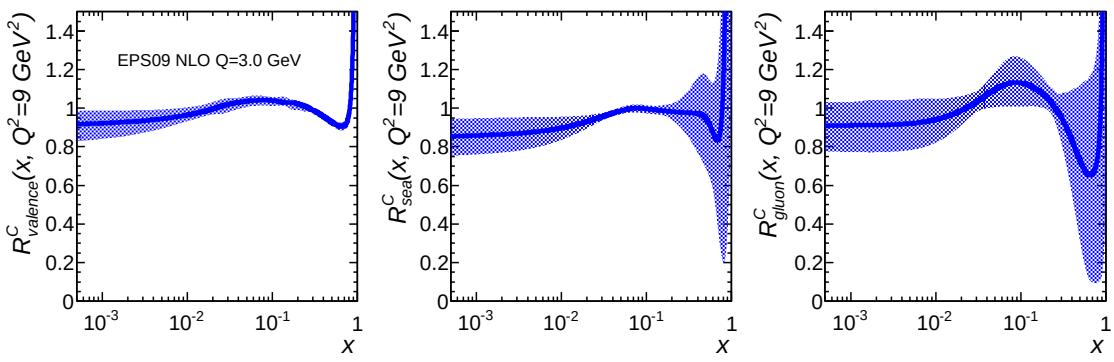

Figure 1.5: Modifications of PDFs for a C nucleus at $Q = 9$ GeV^2 from EPS09 in NLO.

1.3.3 Absorption

A pre-resonance $c\bar{c}$ pair and a J/ψ meson to be formed can be "absorbed" by interactions with the nuclear matter as it traverses a nucleus. This phenomenon is often called "absorption", but it is actually "break-up" because both the charm quark and the charm antiquark still exist even though they become an uncorrelated pair. In the framework of the Glauber model, the survival probability of the J/ψ in pA collisions is expressed as

$$S^{J/\psi}_{\rm abs} = \frac{\sigma^{J/\psi}_{pA}}{A\sigma^{J/\psi}_{pN}} = \frac{1}{A}\int d^2b \int_{-\infty}^{\infty} dz \rho_A(b,z) S^{J/\psi}_{\rm abs}(b,z), \tag{1.5}$$

with

$$S^{J/\psi}_{\rm abs}(b,z) = \exp\left(-\int_z^{\infty} dz' \rho_A(b,z')\sigma^{J/\psi}_{\rm abs})\right), \tag{1.6}$$

where b is the impact parameter of a collision, z is the $c\bar{c}$ production point along the beam axis, ρ_A is the nuclear density, and $\sigma^{J/\psi}_{\rm abs}$ is the absorption cross section [30].

The absorption cross section $\sigma^{J/\psi}_{\rm abs}$ is generally estimated based on the ratio of measured production cross sections of the J/ψ to predicted production cross sections by a theory. The production cross section predicted by a theory depends on models of the PDF, and thus the absorption cross section has a large theoretical error [30].

1.4 Nonperturbative charm component in a nucleon

In general, charm quarks and charm antiquarks in a nucleon are generated through the perturbative process, gluon splitting $g \rightarrow c\bar{c}$. Thus, the PDF for the charm quark at the initial scale is assumed to be zero and it becomes non-zero at a given higher scale than the initial scale after the perturbative QCD evolution. However, there are no reasons nonperturbatively generated charm quarks do not exist in a nucleon. These intrinsically included charm component in a nucleon has been called "intrinsic charm", while perturbative charm component originated from the gluon splitting has been called "extrinsic charm" as contrasted with intrinsic charm. In this section, a distinctive feature of intrinsic charm and its effect on the J/ψ production are described. The current status of intrinsic charm search is briefly described.

1.4.1 Intrinsic charm

Intrinsic charm is firstly introduced to account for the unexpected large production cross section of charmed mesons in the forward region [31]. The EMC experiment shows at large-x the larger charm structure function F_2^c, which accounts for the internal structure of the proton about the charm quark and the charm antiquark, than the predictions based solely on a perturbative QCD [32]. After that, intrinsic charm has been taken seriously as an additional and nonperturbative component of F_2^c to account for the discrepancy between the data and the perturbative component predicted by a perturbative QCD theory.

A striking feature of intrinsic charm is that it is expected to have large-x, while extrinsic charm tends to have small-x which is softer than a gluon distribution because it originates from the gluon splitting. Figure 1.6 shows the charm distributions at scale $Q = 3.0$ GeV for the perturbative component and two well-known intrinsic charm models described later. Both models for intrinsic charm predict a peak in the charm distribution at large-$x \sim 0.3$.

The total production cross section of J/ψ mesons from intrinsic charm in pp collisions can be written as [34]

$$\sigma^{\mathrm{IC}}_{J/\psi,\ pp} = f_{J/\psi} P_{\mathrm{IC}} \sigma^{\mathrm{inel}}_{pp} \frac{\mu^2}{4\hat{m}_c{}^2}, \tag{1.7}$$

where $f_{J/\psi}$ is the probability to produce a J/ψ meson from an intrinsic $c\bar{c}$ state, P_{IC} is the probability of intrinsic charm state $c\bar{c}$ in a proton, $\sigma^{\mathrm{inel}}_{pp}$ is the inelastic cross section for pp collisions, the soft interaction parameter, μ^2, is ~ 0.1 GeV^2 [35], and the average transverse mass, $\hat{m}_c = \sqrt{m_c^2 + \langle k_T^2 \rangle}$, is 1.8 GeV/$c^2$ [35]. In pA collisions, the mass number dependence of the production cross section of J/ψ via

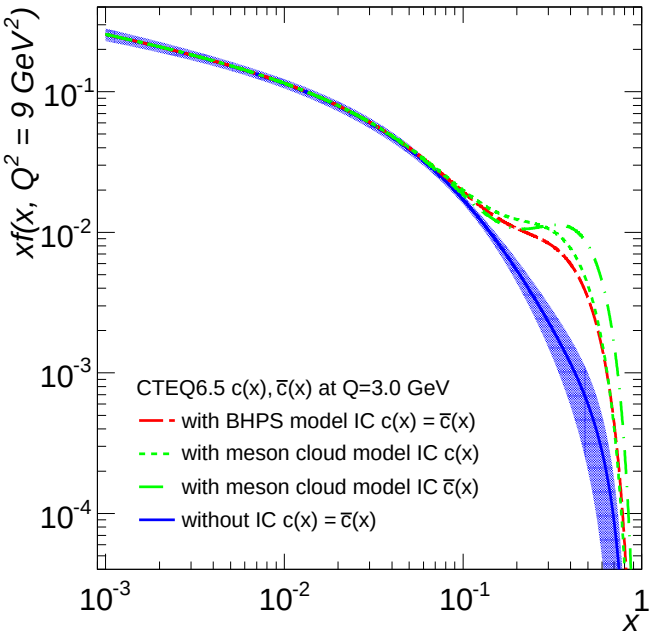

Figure 1.6: Charm quark distributions from two intrinsic charm models (the BHPS model and the meson cloud model) and the perturbative component at scale $Q = 3.0$ GeV. The amount of intrinsic charm $\langle x \rangle_{c+\bar{c}} = \int_0^1 x[c(x)+\bar{c}(x)]dx$ is 0.57% for the BHPS model and 0.96% for the meson cloud model, which is based on CTEQ6.5 [33].

intrinsic charm is considered to be $A^{2/3}$ [36] and the cross section is expressed as $\sigma^{\rm IC}_{J/\psi,\ pA} = A^{2/3}\sigma^{\rm IC}_{J/\psi,\ pp}$. The size of the J/ψ can be estimated as

$$r_{J/\psi} \sim (2m_D - m_{J/\psi})^{-1} \sim 0.25 \text{ fm}, \tag{1.8}$$

and this size is sufficiently smaller than the typical hadronic size $\Lambda^{-1}_{\rm QCD} \sim 1$ fm. The intrinsic $c\bar{c}$ state passes through a target nucleus due to its small spatial extent, whereas the light spectator quarks which are remnants of the nucleon after the $c\bar{c}$ emission have small momenta interact on the nuclear surface of the target because the most of the nucleon momentum is carried by the $c\bar{c}$.

1.4.2 Intrinsic charm models

Two well-known models for describing the origin of intrinsic charm and its PDF are briefly introduced.

BHPS model

The BHPS model was proposed in 1980 [31], named after its authors. In this model, intrinsic charm is included in $|uudc\bar{c}\rangle$ Fock state fluctuation of the nucleon wavefunction. The wavefunction of a proton, for example, is expressed as a superposition of Fock components

$$|p\rangle = \psi_{uud}\,|uud\rangle + \psi_{uudg}\,|uudg\rangle + \psi_{uudq\bar{q}}\,|uudq\bar{q}\rangle + \psi_{uudc\bar{c}}\,|uudc\bar{c}\rangle + \cdots, \tag{1.9}$$

where q represents a light quark and ψ represents the wave function amplitude of each Fock component. Intrinsic charm is expected to be generated nonperturbatively by virtual interaction such as $gg \to c\bar{c}$ where the gluons couple to two or more valence quarks in a proton unlike "extrinsic charm" generated perturbatively by the gluon splitting $g \to c\bar{c}$. Figure 1.7 shows the diagrams of production of intrinsic charm in this model and extrinsic charm in the ordinary QCD evolution. The probability for five-quark intrinsic $c\bar{c}$ state as a function of the momentum fraction x and the transverse momentum k_T is simply assumed as [34]

$$\frac{dP_{\rm IC}}{\prod_{i=1}^{5} dx_i d^2k_{T,i}} = N_5 \frac{\delta(\sum_{i=1}^{n} \boldsymbol{k}_{T,i})\delta(1 - \sum_{i=1}^{5} x_i)}{(m_p^2 - \sum_{i=1}^{5}(m_{T,i}^2/x_i))^2}, \tag{1.10}$$

where N_5 normalizes the Fock state probability, m_p is the proton mass, $m_{T,i}$ is the transverse mass of a quark ($\sqrt{m_i^2 + \boldsymbol{k}_{T,i}^2}$), and i = 1–5 represent up quark, up quark, down quark, charm quark, and charm antiquark, respectively. The x distribution of intrinsic charm in the proton is obtained by integrating this equation over all x's

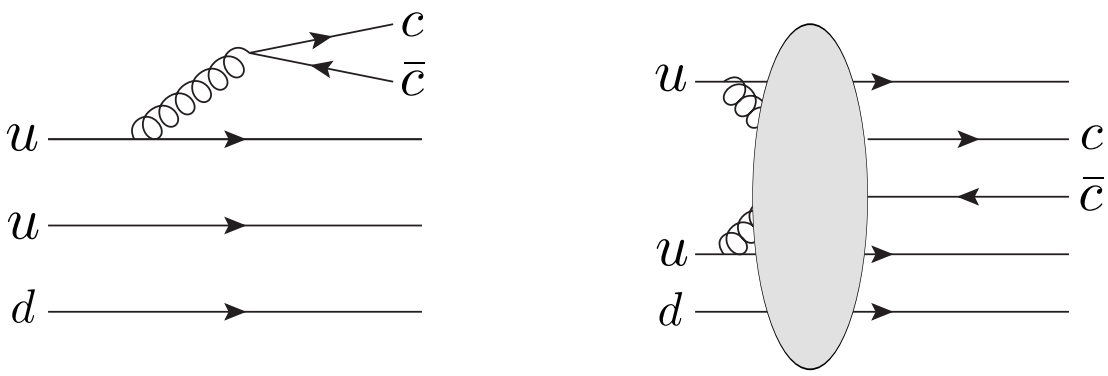

Figure 1.7: Diagram of extrinsic charm production (left panel) and a diagram of intrinsic charm production (right panel).

except for x_4, the charm quark. The BHPS model assumes $m_c = m_{\bar{c}} \gg m_p, m_u, m_d$ and neglects the effect of the transverse momentum. Then, the PDF of intrinsic charm is expressed as

$$c_{\rm IC}(x) \propto x^2 \left((1-x)(1+10x+x^2) + 6x(1+x)\ln x\right). \tag{1.11}$$

In this model, the PDF of intrinsic charm antiquark has the same shape as the charm distribution: $\bar{c}_{\rm IC}(x) = c_{\rm IC}(x)$. It should be noted that this nonperturbatively generated intrinsic charm must evolve according to a leading twist as extrinsic charm which is perturbatively generated. Regardless of its origin, the intrinsic charm and extrinsic charm are affected by the same QCD correction. In general, the PDF of intrinsic charm in Eq. 1.11 is implemented at the initial scale μ of the PDF, instead of $c(x,\mu) = \bar{c}(x,\mu) = 0$. The charm distribution from extrinsic charm and intrinsic charm based on the BHPS model at scale $Q = 3.0$ GeV is shown in Fig. 1.6.

Meson cloud model

An alternative to the BHPS model was proposed in Ref. [37, 38, 39]. In this model, intrinsic charm arises from the fluctuation of a nucleon to a virtual $D+\Lambda_c^+$ state. For the proton, it is expressed as $p \to \bar{D}^0 + \Lambda_c^+$ and $n \to D^- + \Lambda_c^+$ for the neutron. The PDF for the charm quark can be obtained with the convolution of the distribution of Λ_c^+ in the nucleon and the charm distribution in Λ_c^+. The same picture can be applied to the charm antiquark.

The PDF of the charm quark in a nucleon in light-cone frame (infinite-momentum

frame) can be expressed as

$$\begin{aligned} \bar{c}(x) &= \int_x^1 \frac{dz}{z} f_{D/N}(z) \bar{c}_D(\frac{x}{z}), \\ c(x) &= \int_x^1 \frac{dz}{z} f_{\Lambda_c/N}(z) c_{\Lambda_c}(\frac{x}{z}), \end{aligned} \tag{1.12}$$

where z is the fraction of the nucleon's light-cone momentum carried by the D or Λ_c. The light-cone distribution of the D meson in a nucleon is given by

$$\begin{aligned} f_{D/N}(z) &= \frac{g^2_{ND\Lambda_c}}{16\pi^2} \int_0^\infty dk_\perp^2 \frac{F^2(k_\perp^2, z)}{z(1-z)(s_{D\Lambda_c} - m_N^2)^2} \frac{k_\perp^2 + (m_{\Lambda_c} - (1-z)m_N)^2}{1-z}, \\ F^2(k_\perp^2, z) &= \frac{\Lambda^2 + m_N^2}{\Lambda^2 + s_{D\Lambda_c}}. \end{aligned} \tag{1.13}$$

The light-cone distribution of the Λ_c can be obtained using $f_{\Lambda_c/N}(z) = f_{D/N}(1-z)$. In Eq. 1.13, $g_{ND\Lambda_c}$ denotes the $ND\Lambda_c$ coupling constant, $s_{D\Lambda_c}$ is the $D\Lambda_c$ center of mass energy squared, $F^2(k_\perp^2, z)$ is a form factor at $ND\Lambda_c$ vertex, and Λ is a cut-off parameter for the form factor. The coupling constant is estimated with a QCD sum rule calculation [40].

The charm antiquark distribution in the D and the charm quark distribution in the Λ_c can be approximated as

$$\begin{aligned} \bar{c}_{D/N}(x) &= \delta(x-1), \\ c_{\Lambda_c/N}(x) &= \delta(x - 2/3), \end{aligned} \tag{1.14}$$

due to the large mass of the charm quark compared to the up quark and the down quark. With this approximation, the PDF of intrinsic charm is written as

$$\begin{aligned} \bar{c}(x) &= f_{D/N}(x), \\ c(x) &= \frac{3}{2} f_{\Lambda_c/N}(3x/2). \end{aligned} \tag{1.15}$$

In this meson cloud model, the asymmetric charm quark and charm antiquark distribution can be naturally introduced, while the BHPS model assumes the same distribution for the charm quark and the charm antiquark. The charm distribution from intrinsic charm based on the meson cloud model at scale $Q = 3.0$ GeV is shown in Fig. 1.6.

As mentioned above, it should be noted that this nonperturbatively generated intrinsic charm must evolve according to a leading twist as extrinsic charm which is perturbatively generated.

1.4.3 Charm structure function

Intrinsic charm reflects nonperturbative structure of a nucleon. Thus, it can be probed by DIS experiments. The scattering cross section for the DIS reaction $e^-(l_1) + p(p) \rightarrow e^-(l_2) + c + X$ can be written in terms of the structure functions $F_2^c(x, Q^2)$ and $F_L^c(x, Q^2)$ as

$$\frac{d^2\sigma^c}{dxdQ^2} = \frac{2\pi\alpha^2(Q^2)}{xQ^4}\left[(1+(1-y)^2)F_2^c(x,Q^2) - y^2F_L^c(x,Q^2)\right], \tag{1.16}$$

where $Q^2 = -q^2 \equiv -(l_1 - l_2)^2$, $x = Q^2/2p \cdot q$ is the Bjorken scaling variable and $y = p \cdot q/p \cdot l_1$ represents the inelasticity of the reaction with p, q, l_1, and l_2 denoting the 4-momenta of the proton, photon, incident electron, and outgoing electron, respectively. If intrinsic charm exists, the charm production cross section σ^c is expected to be enhanced in large-x region.

The charm structure function F_2^c was measured by the EMC through dimuon events produced by the interaction of a muon beam at 250 GeV with an iron target ($\mu^+\text{Fe} \rightarrow \mu\mu X$) [32]. Muons in the final state consist of a scattered incident muon and a decay product of the semileptonic decay of a D meson. Figure 1.8 shows the observed charm structure function F_2^c, together with perturbative QCD predictions at LO. A significant excess of the data from the perturbative QCD prediction at large-x was observed. This excess has been examined in terms of intrinsic charm contribution by many studies as described later. In an experimental extraction of F_2^c from σ^c, the F_L^c contribution was either neglected or approximated by LO QCD.

The H1 and ZEUS collaborations at HERA also measured the charm structure function in ep DIS with higher precision than the EMC [41]. The kinematic range is $2.5 \leq Q^2 \leq 2000$ GeV^2 and $3 \cdot 10^{-5} \leq x \leq 5 \cdot 10^{-2}$. The charm structure function at large-x is not so extensively studied as the EMC and thus the HERA data is less sensitive to intrinsic charm contribution. However, the HERA data is very precise in the small-x region and is used by global QCD analyses described later to check the overall consistency of the charm structure function with an intrinsic charm scenario.

1.4.4 Current status on intrinsic charm

Despite a number of studies to evaluate the amount of intrinsic charm in a nucleon P_{IC} [31, 33, 42, 43, 44, 45, 46, 47], the amount of intrinsic charm in a nucleon, even its existence, is still controversial. The amount of intrinsic charm is defined as

$$P_{\text{IC}} = \int_0^1 dxc(x). \tag{1.17}$$

Evaluation of the P_{IC} strongly depends on intrinsic charm production model and the charm structure function which depends on the input data.

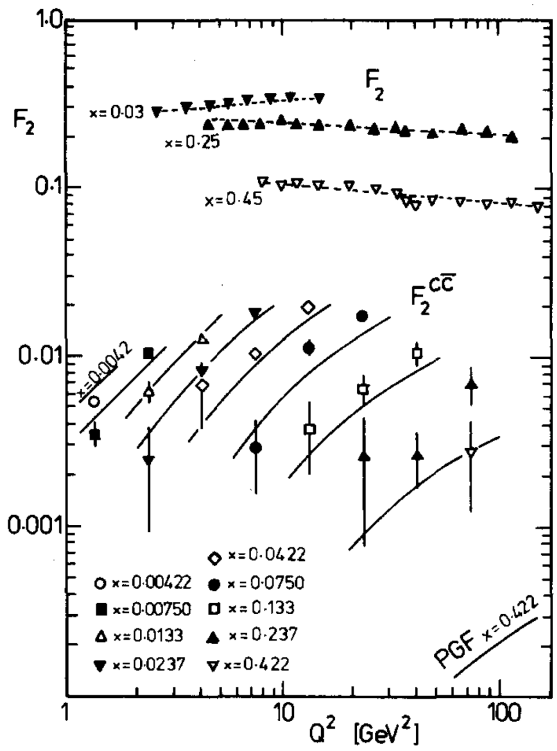

Figure 1.8: Charm structure function F_2^c obtained by the EMC [32] as a function of Q^2 for fixed x, together with the predictions from a perturbative QCD at LO. Taken from Fig. 14 in Ref. [32].

The probability $P_{\rm IC}$ was initially suggested to be ∼1% [31]. Then, the EMC measured the charm structure function and provided a positive result for the presence of intrinsic charm. The $P_{\rm IC}$ evaluated from the EMC data ranges 0.3–0.86% [42,43,46]. With combination of the EMC and HERA data, 0.4–0.75% was obtained [44], depending on intrinsic charm models. Global QCD analyses of the PDFs were also performed and the results ranges from zero to 3% [33, 45, 46], while an effective theory predicted $P_{\rm IC} = 0.6\%$ [47]. Here, the studies to evaluate the $P_{\rm IC}$ are briefly introduced.

Brodsky *et al.* [31]

Intrinsic charm was firstly introduced in Ref. [31] and $P_{\rm IC}$ was estimated to be ∼ 1%. The probability was roughly estimated from the data of the total diffractive cross section of pp collisions and the cross sections for D^+ and Λ_c^+ production. The single diffractive cross section of pp collisions ($pp \to pX$) is ∼ 8 mb at $\sqrt{s} \approx$ 30–40 GeV [48], while the cross section for the charm production is 100–500 µb at $\sqrt{s}$ =53 and 63 GeV [49,50,51,52]. They assumed that the most of the charm production came from the diffractive process. Then, the probability $P_{\rm IC}$ can be defined as the ratio of the cross section for the charm production to the total diffractive cross section, resulting in $P_{\rm IC}$ ∼1%.

Hoffmann and Moore *et al.* [42]

The probability $P_{\rm IC}$ was obtained by comparing the charm structure function F_2^c measured by the EMC to F_2^c calculated by a theory. The contributions to the charm structure function of extrinsic charm and intrinsic charm were calculated separately. The BHPS model was used as an intrinsic charm model.

Extrinsic charm contribution to the structure function was estimated in the framework of the photon-gluon fusion approach (PGF). In this framework, an extrinsic charm quark pair is only created through photon-gluon fusion process ($\gamma^* g \to c\bar{c}$) at the lowest order in a nucleon, and the structure function due to this process is given by,

$$F_2^{c\ \rm PGF}(x,Q^2) = e_c^2 \frac{\alpha_s(\mu^2)}{4\pi} \int_x^{z_{max}} dz H_g(z,Q^2,m_c^2 c) \frac{x}{z} g(\frac{x}{z},\mu^2), \tag{1.18}$$

where e_c is the charge of a charm quark, μ^2 is the renormalization scale, H_g is the partonic cross section for producing a charm quark pair, g is the gluon distribution, and $z_{max} = 1/(1 + 4m_c^2/Q^2)$. Once, μ^2 is fixed, the gluon distribution itself is not evolved from the initial scale in the PGF framework, but rather the partonic cross section depends on a given energy scale. The gluon distribution used in this

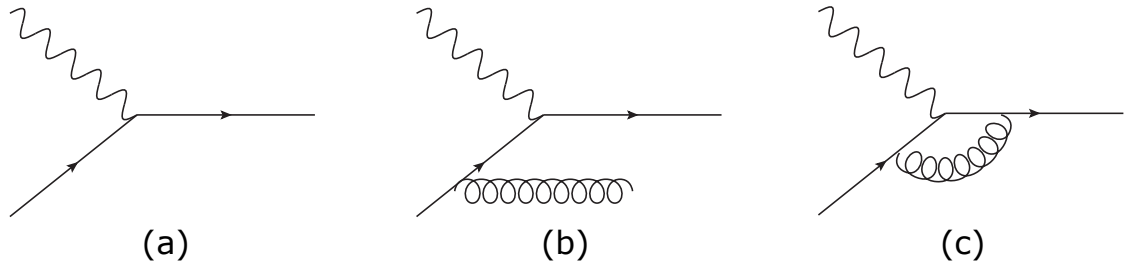

Figure 1.9: (a) Zeroth order photon-quark scattering diagram. (b) $\mathcal{O}(\alpha_s)$ correction to the intrinsic charm distribution due to gluon Bremsstrahlung. (c) $\mathcal{O}(\alpha_s)$ correction to the intrinsic charm distribution due to a virtual gluon.

calculation was based on Ref. [53] at LO and the nuclear shadowing effects were not incorporated.

The contribution of intrinsic charm to the structure function was calculated, considering the zeroth order photon-quark scattering and the $\mathcal{O}(\alpha_s)$ corrections to it due to gluon Bremsstrahlung and virtual gluons. The diagrams of these processes are shown in Fig. 1.9. Furthermore, they incorporated an effect of the charm quark mass and proton mass into the charm structure function. The values of Q^2 covered by the EMC data ranges from 2 GeV^2 to 80 GeV^2. In this scale, the charm quark mass ($m_c^2 \sim 2$ GeV^2) can not be neglected. Thus, simple form of the charm structure function $F_2^{c\ \mathrm{IC\ LO}}(x) = 8xc(x)/9$ should be modified, where $c(x)$ is the PDF of intrinsic charm expressed as Eq. 1.11. The modified charm structure function at LO due to the mass effect is expressed as

$$F_2^{c\ \mathrm{IC\ LO}}(x, Q^2) = \frac{8x^2}{9(1+4\rho x^2)^{3/2}} \left(\frac{1+4\lambda}{z} c(z,\gamma) + \hat{g}(z,\gamma) \right), \tag{1.19}$$

where

$$
\begin{aligned}
c(z,\gamma) &= \begin{cases} c(z) - \frac{z}{\gamma}c(\gamma) & (z \le \gamma) \\ 0 & (z \ge \gamma), \end{cases} \\
\hat{g}(z,\gamma) &= \frac{2\rho x}{1+4\rho x^2}\int_z^\gamma dt \frac{c(t,\gamma)}{t}\left(1-\frac{\lambda}{\rho t^2}\right)\left(1+2\rho x t+\frac{2\lambda x}{t}\right), \\
z &= \frac{2ax}{1+\sqrt{1+4\rho x^2}}, \\
\rho &= m_p^2/Q^2, \\
\lambda &= m_c^2/Q^2, \\
a &= \frac{\sqrt{1+4\lambda}+1}{2}, \\
\gamma &= \frac{2a\hat{x}}{1+\sqrt{1+4\rho\hat{x}^2}}, \\
\hat{x} &= \frac{1}{1+4\lambda-\rho}.
\end{aligned}
\tag{1.20}
$$

The NLO correction to the charm structure function due to intrinsic charm is written as,

$$
F_2^{c\ \mathrm{IC\ NLO}}(x,Q^2) = \frac{8}{9}z\int_z^\gamma \frac{dy}{y}c(y,\gamma)\sigma^{\mathrm{NLO}}(z/y,\lambda), \tag{1.21}
$$

where σ^{NLO} denotes the $\mathcal{O}(\alpha_s)$ corrections to a photon-charm quark scattering cross section due to the diagrams shown in Fig. 1.9. It should be noted that the charm distribution itself is not evolved from the initial scale in this framework, but rather the partonic cross section depends on a given energy scale.

Finally, the total charm structure function was written as

$$
F_2^c = F_2^{c\ \mathrm{PGF}} + F_2^{c\ \mathrm{IC\ LO}} + F_2^{c\ \mathrm{IC\ NLO}}. \tag{1.22}
$$

With this scheme, P_{IC} was evaluated to be 0.31% as shown in Fig. 1.10. This calculation included the LO contribution of extrinsic charm to the charm structure function based on the PGF and the NLO contribution of intrinsic charm based on the BHPS model.

Harris *et al.* [43]

They extended the analysis performed by Ref. [42] on the EMC charm production data by calculating the NLO extrinsic and intrinsic charm contribution to the charm structure function, while the LO calculation on extrinsic charm had been performed in Ref. [42]. The NLO contribution of extrinsic charm includes a charm quark pair

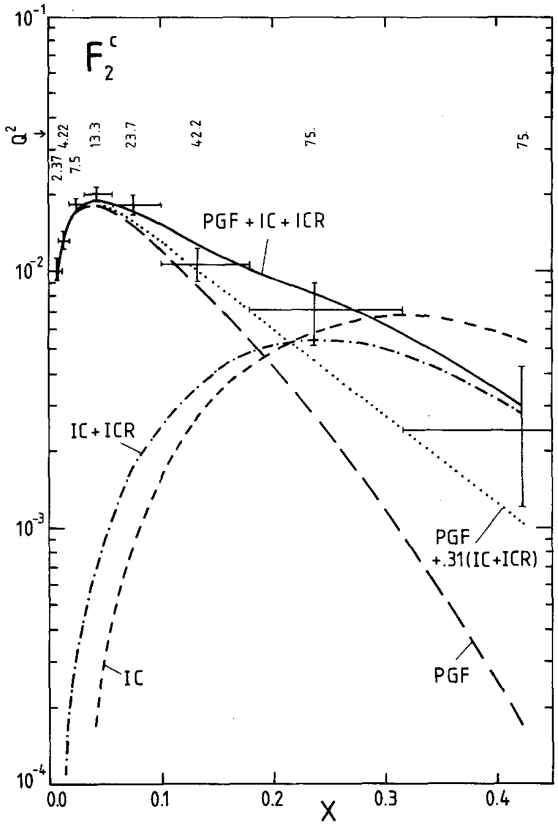

Figure 1.10: Comparison of the charm structure function F_2^c between the measured result by the EMC [32] and the theoretical prediction with intrinsic charm as a function of x. The data points are a subset of the all EMC data: for a given value of x, the data point with the highest associated Q^2 is plotted. Taken from Fig. 7a in Ref. [42].

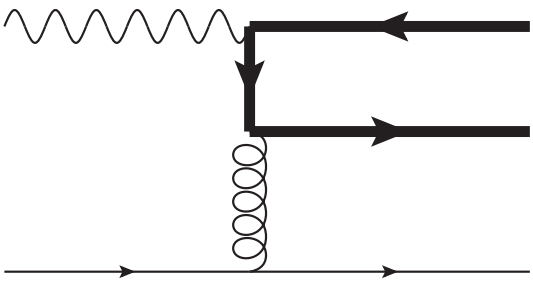

Figure 1.11: Charm quark pair production by a light quark. Heavy solid lines represent a charm quark and a charm antiquark, while light solid lines represent a light quark.

production from light quarks as shown in Fig. 1.11. For light quark distributions as well as a gluon distribution, they used three models of PDFs (CTEQ3, MRS(G), and GRV94). The nuclear shadowing effects were not incorporated. The $P_{\rm IC}$ was obtained by fitting the EMC data with the theoretical predictions including intrinsic charm contribution. Figure 1.12 shows the fit results and $P_{\rm IC}$ was found to be $0.86 \pm 0.60\%$.

Steffens *et al.* [44]

The probability $P_{\rm IC}$ was obtained by comparing the measured charm structure functions F_2^c by the EMC and the H1 and ZEUS collaborations at HERA with that of a theoretical calculation at NLO. The data from HERA probed small-x region down to $x = 3 \times 10^{-5}$ and less sensitive to intrinsic charm contribution which is expected to appear in large-x region. However, the data from HERA is very precise in small-x region and overall consistency between the data and a theoretical prediction on the charm structure function can be checked. In this calculation, the meson cloud model was also used as the intrinsic charm production model, as well as the BHPS model. At a given scale, the intrinsic charm distribution was evaluated according to the QCD evolution as well as the extrinsic charm distribution and then the charm structure function was estimated based on these distributions. This is completely different from the former analyses [42, 43]. The parametrization of GRV [54] and MRST [55] were used. The nuclear shadowing effects were not incorporated.

The charm structure function was calculated based on the hybrid of the PGF and massless evolution scheme (VFNS), which is called interpolating scheme (IS). In the PGF, the charm structure function Eq. 1.18 includes $\log(Q^2/m_c)$ in H_g and this term could be problematic at very large Q^2. Thus, the massless evolution scheme was introduced. In this scheme, the charm distribution is $c(x, \mu^2) = \bar{c}(x, \mu^2) = 0$ below

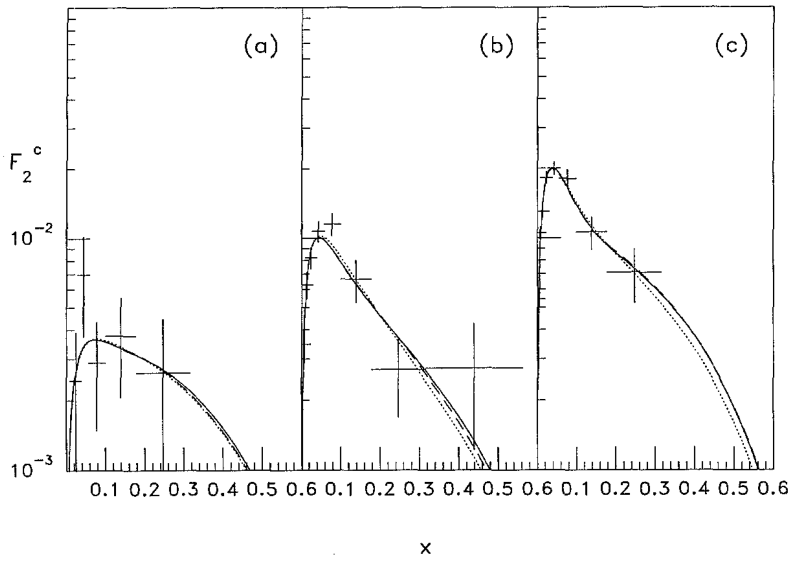

Figure 1.12: (a) Comparison of the charm structure function F_2^c between the measured result by the EMC [32] and the theoretical prediction including the intrinsic charm contribution as a function of x at $\bar{\nu} = 53$ GeV, where ν is the energy difference of an incident muon and a scattered muon. The solid line is for the CTEQ3, the dotted line is for the MRS(G), and the dashed line is for the GRV94. (b) Same as (a) for $\bar{\nu} = 95$ GeV. (c) Same as (a) for $\bar{\nu} = 168$ GeV. Taken from Fig. 7 in Ref. [43].

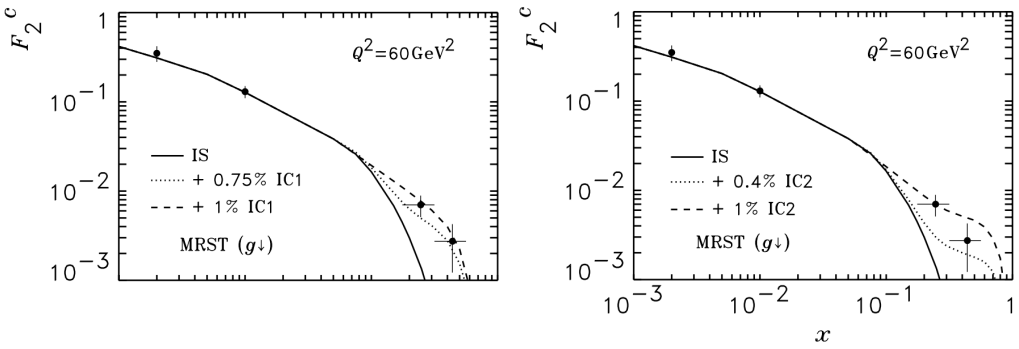

Figure 1.13: Left panel: Comparison of the charm structure function F_2^c between the measured results and the theoretical prediction with BHPS intrinsic charm (IC1) and the MRST parametrization [55] with the minimum gluon. Right panel: Same as left panel, but with meson cloud model of intrinsic charm (IC2). Based on Fig. 8 in Ref. [44].

the initial scale μ and evolve charm quarks as massless partons. This scheme well describes the charm structure function at large Q^2, but do not in the region around m_c^2 in contrast to the PGF. Thus, the hybrid approach IS was used to calculate the charm structure function. The results were $P_{\mathrm{IC}} = 0.75\%$ for the BHPS model and $P_{\mathrm{IC}} = 0.4\%$ for the meson cloud model as shown in Fig. 1.13.

Martin *et al.* [45]

The probability P_{IC} was obtained by comparing the measured charm structure function F_2^c by the EMC with a theoretical calculation. It should be noted that the main purpose of Ref. [45] is to determine the PDFs and based on many DIS experiments, including the data from HERA. When it referees to intrinsic charm analysis, however, the EMC data was exclusively used and HERA data was not used. The charm structure function was calculated at NLO based on GM-VFNS, described in detail in Ref. [45]. The results were $P_{\mathrm{IC}} = 0.3\%$ for the BHPS model as shown in Fig. 1.14.

Pumplin *et al.* [33]

A global QCD analysis of PDFs was performed. The extrinsic charm contribution to the charm structure function was calculated based on the PDF of CTEQ6.5M [56]. Both the BHPS model and meson cloud model were used as an intrinsic charm production model. The probability P_{IC} ranges from zero to 3%.

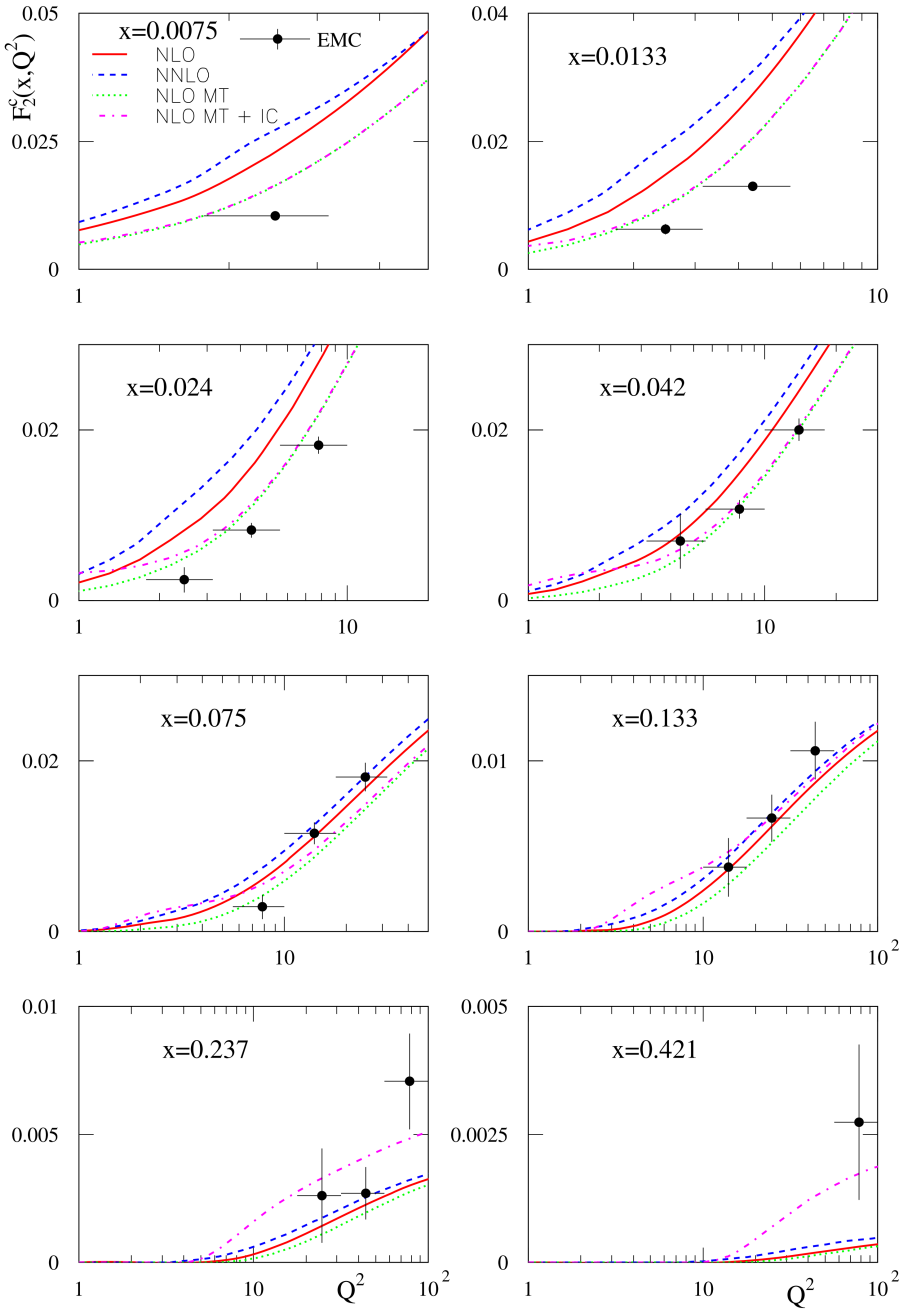

Figure 1.14: Comparison of the charm structure function F^{c_2} between the measured result by the EMC [32] and the theoretical prediction with intrinsic charm as a function of x. Abbreviations of MT and IC stand for the modified threshold approach (details are given in Ref. [45]) and intrinsic charm, respectively.

Jimenez-Delgado *et al.* [46]

A global QCD analysis of PDFs was performed. The charm structure function was decomposed into perturbative ($F_2^{c\bar{c}}$) and nonperturbative components (F_2^{IC}),

$$F_2^c = F_2^{c\bar{c}} + F_2^{\mathrm{IC}}. \tag{1.23}$$

The perturbative component is equivalent to extrinsic charm and the nonperturbative component is equivalent to intrinsic charm. The perturbative component was calculated at NLO based on the PGF using the gluon and light quark distributions of JR14 global fit [57] with the nuclear shadowing effects [58]. The nonperturbative component was calculated at NLO using the meson cloud model [39] based on the framework of Hoffmann and Moore [42]. In this global QCD analysis, there is a significant tension between the HERA data and the EMC data in regions of overlapping kinematics. The results strongly depends on the input data sets and treatment of the tension. The authors concludes $\langle x \rangle_{\mathrm{IC}} = 0.15 \pm 0.09\%$ and $\langle x \rangle_{\mathrm{IC}} \approx 0.5\%$ at most at the 4σ level. This results are obtained without the EMC data, while the EMC data alone favored a value $\sim$(0.3–0.4)%.

Duan *et al.* [47]

The probability of P_{IC} was calculated with the extended chiral constituent quark model [59]. Instead of the indirect approach using the charm structure function, this method directly calculated the probability by assuming the interactions between constituent quarks in a nucleon based on the Yukawa interaction potential $V_M(r_{ij})$, where $V_M(r_{ij})$ represents the M meson-exchange interaction between the ith and jth quarks. The nucleon wavefunction was expressed as

$$|\Phi\rangle_N = \frac{1}{\sqrt{\mathcal{N}}} \left(|qqq\rangle + \sum_{i,n_r,l} C_{in_rl} \, |qqq(Q\bar{Q}), i, n_r, l\rangle \right), \tag{1.24}$$

where the first term represents the conventional wave function for the nucleon with three constituent quarks and the second term is a sum over higher Fock components with a $Q\bar{Q}$ pair: $Q\bar{Q} \equiv u\bar{u}$, $d\bar{d}$, $s\bar{s}$, or $c\bar{c}$. The result was $P_{\mathrm{IC}} = 0.6 \pm 0.1\%$.

1.5 J/ψ production in fixed target experiments

Production cross section of the J/ψ in pA collisions has been measured by many experiments (Appendix A), covering the center of mass energy ranges $\sqrt{s}$ $\approx$6.8–52 GeV. At low energy, the J/ψ production cross section in pA collisions is simply assumed to follow a power law

$$\sigma_{pA} = A^{\alpha} \sigma_{pp}, \tag{1.25}$$

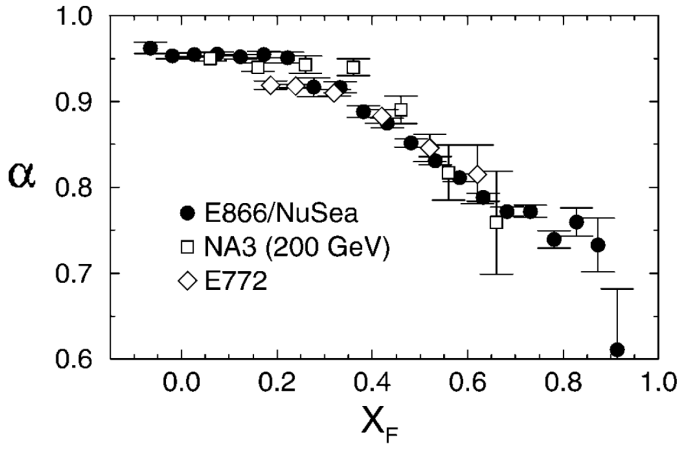

Figure 1.15: Suppression factor α versus x_F for the J/ψ from E866 (solid circles) compared to E772 (open diamonds) and NA3 (open squares). Taken from Fig. 4 in Ref. [60].

where the parameter α represents the nuclear dependence. A value of $\alpha < 1$ indicates the suppression of the J/ψ production in pA collisions compared to pp collisions due to the nuclear effects, whereas a value of $\alpha > 1$ means the enhancement.

The anomalous J/ψ suppression at large Feynman-x region (x_F) was observed in pA collisions [60, 61, 62, 63]. The Feynman-x given by $x_F = x_1 - x_2$, where x_1 is x-value of the projectile and x_2 is x-value of the target. The forward region corresponds to $x_F > 0$ and the backward region corresponds to $x_F < 0$, while $x_F = 0$ maps to $y = 0$, where y is the rapidity. Figure 1.15 shows the x_F dependence of the α parameter. Two clear trends are observed. First, the suppression is observed in the whole range $x_F > 0$. Second, the suppression factor α decreases toward $\sim 2/3$ as x_F increases. If the J/ψ is produced by conventional hard processes, this suppression pattern suggests only J/ψ produced in the forward region strongly interacts with the nuclear matter. These results contradict the high color-transparency of the J/ψ due to its smallness. Furthermore, the suppression pattern also contradicts perturbative QCD factorization [64]. If this suppression is attributed to the nuclear shadowing or radiative energy loss of an incident parton, the same suppression pattern should be observed in DY dilepton yield in the same x_F region. Figure 1.16 shows the ratios of the dimuon yield per nucleon for an iron target to an beryllium target (Fe/Be) and to an carbon target (Fe/C) from DY process [65,66]. The suppression factor α stays ~ 0.95 even at the most forward region. Thus, the suppression of the J/ψ can not be interpreted as a result of the nuclear shadowing nor radiative energy loss. One possible explanation is the contribution of intrinsic charm to the J/ψ production. The mass number dependence of the production cross section of the J/ψ via intrinsic

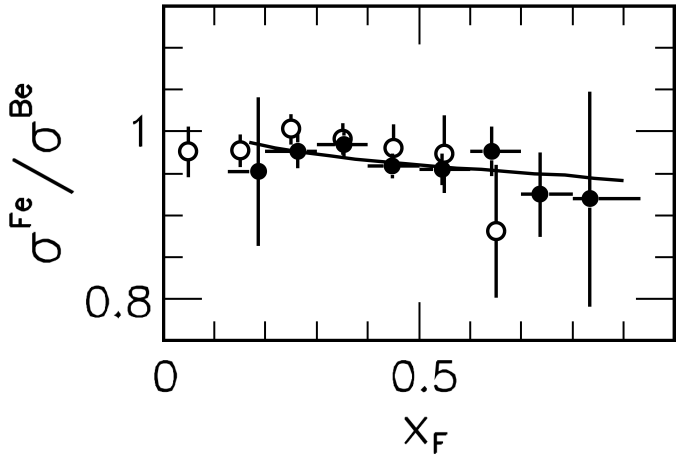

Figure 1.16: Ratios of the dimuon yield from DY process per nucleon as a function of x_F from E886 (solid circles, Fe/Be) and E772 (open circles, Fe/C). Based on Fig. 1 in Ref. [65].

charm is considered to be $A^{2/3}$ [36] (Sec. 1.4.1). The J/ψ from intrinsic charm will be produced in large-x_F, because the intrinsic charm quark distribution in a nucleon is expected to peak at large-$x \sim 0.3$. Thus, if there is a significant contribution from intrinsic charm to the J/ψ production, the mass number dependence of the J/ψ in the large-x_F region approaches $\alpha = 2/3$. This picture is consistent with the observed suppression pattern of the J/ψ in the large-x_F region.

1.6 Physics motivation

This thesis is dedicated to the analysis of the production cross section of the J/ψ meson in 12 GeV pA reactions, corresponding to the center of mass energy $\sqrt{s} = 5.1$ GeV. This is the lowest energy experiment for the J/ψ production by hadron interactions in all the experiments ever conducted. Actually, $\sqrt{s} = 5.1$ GeV is just above the threshold of the simplest final state ppJ/ψ, which is 4.97 GeV. Therefore one expects that the results of this study can provide crucial information on contributions of nonperturbative processes to the J/ψ production by hadron interactions. If there is a contribution of intrinsic charm, whose existence has not been established, to the J/ψ production in pA collisions, the contribution will appear at large-$|x_F|$ regions. Our spectrometer covers the backward region down to $x_F = -1$. Thus, this analysis is also suitable for the study on intrinsic charm. The data for this analysis has been obtained at KEK 12 GeV PS in 2001 and 2002 by the KEK-PS E325 experiment, which has measured the dielectron mass spectra. The spectrom-

eter has been constructed at the primary beamline EP1-B in PS to detect vector mesons, ρ, ω, ϕ, and J/ψ mesons, decaying into the e^+e^- channel. This high intensity primary beam up to 1×10^9 per spill of two seconds enables the analysis on low-yield dielectron decays from vector mesons.

1.7 Organization of this thesis

The organization of this thesis is as follows. Chapter 2 describes the KEK EP1-B beamline and the spectrometer. Chapter 3 explains the analysis procedure. Chapter 4 presents the results of the production cross section of the J/ψ meson and the interpretation of the obtained results. The conclusions are given in Chapter 5.

1.8 Major contributions

My major contributions as a KEK-PS E325 collaborator are as follows:

Energy calibration of electromagnetic calorimeters: Energy calibration performed for our earlier publications on ρ, ω, and ϕ mesons [67, 68, 69] did not pay particularly close attention to a high momentum electron, because the momentum of e^+e^- tracks from those mesons is relatively low compared to the momentum of e^+e^- tracks from the J/ψ. I have performed re-calibration of the electromagnetic calorimeter for a high momentum electron track.

Development of an event generator for the J/ψ: There is no reliable event generators for the J/ψ at low energy. I have developed an event generator for the J/ψ which well reproduces measured result as described later.

Whole analysis on the J/ψ: The analysis on the dielectron spectra of ρ, ω, and ϕ mesons has already been performed in our earlier publications [67, 68, 69]. This thesis focuses on the J/ψ mass region.

Chapter 2

Experimental setup

2.1 Overview of the apparatus

The spectrometer was constructed at the primary beamline EP1-B in 12 GeV PS at KEK. The beamline EP1-B was constructed in 1995 for providing a high-intensity primary proton beam [70] and was designed to transport 12 GeV protons with the maximum intensity of 4×10^9 per spill of two seconds.

The spectrometer was designed to measure the dielectron mass spectrum and $\phi \to K^+K^-$ with the same apparatus. The schematic view of our spectrometer is shown in Fig. 2.1 and Fig. 2.2. In this thesis, the right-handed coordinate system was used where the origin was at the center of a spectrometer magnet, and the x-axis is parallel to the beam, the z-axis is vertical pointing upward.

The spectrometer consists of a dipole magnet, tracking devices, and two arms for electron and kaon identification. The electron arms cover from $\pm12^\circ$ to $\pm90^\circ$ horizontally and $\pm22^\circ$ vertically, while the kaon arms cover from $\pm12^\circ$ to $\pm54^\circ$ horizontally and $\pm6^\circ$ vertically. The typical acceptance for $J/\psi \to e^+e^-$ is $p_T < 3.2$ GeV/c and $1.0 < y < 2.0$ and the beam rapidity $y_{\rm beam}$ is 3.3. It should be noted that the analysis presented in this thesis does not use the kaon arms. A detailed description of the spectrometer can be found in Ref. [71].

Nuclear targets were placed at the center of the dipole magnet. Primary protons with a typical intensity of 8.7×10^8 and 6.4×10^8 protons per spill were delivered to the targets in 2001 and 2002, respectively. To cope with this high intensity beam, the thin targets were used as the rate of γ conversions inside the targets was lower than the rate of the π^0 Dalitz decay of 1.2%. In 2001, one carbon and two copper targets were installed, while in 2002 one carbon and four copper targets were installed. The interaction length of the carbon target in 2001 and that in 2002 are 0.11% and 0.21%, respectively, and that of each copper target is 0.054%. The typical interaction rate was approximately 1.2 MHz in 2002.

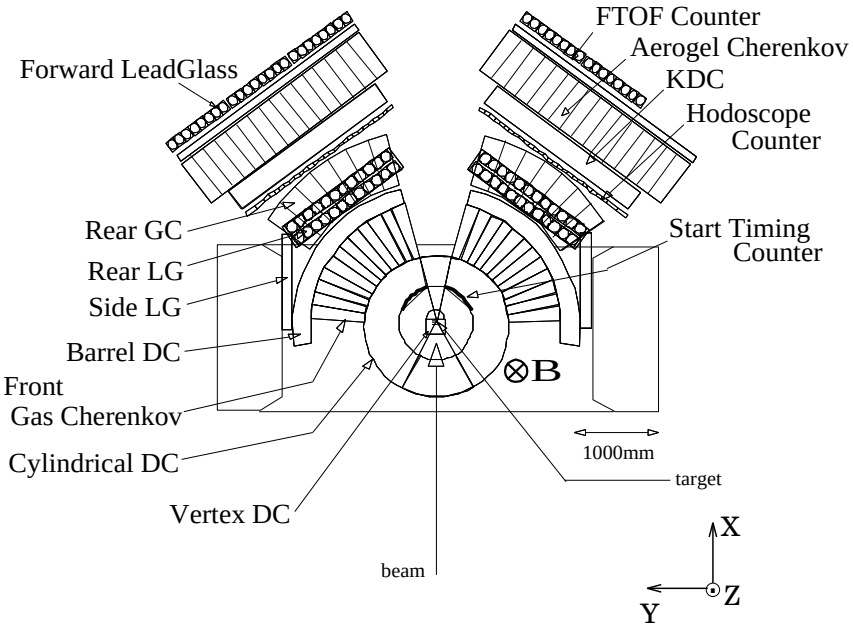

Figure 2.1: Schematic top view of the spectrometer. Based on Fig. 1 in Ref. [71].

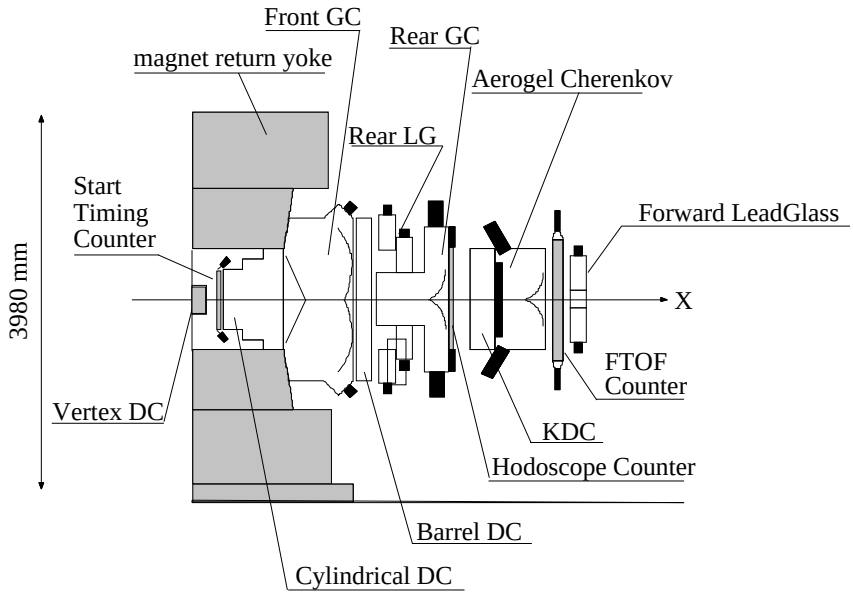

Figure 2.2: Schematic side view of the spectrometer along the center of a kaon arm, corresponding to 33 degrees from the beam line. Based on Fig. 2 in Ref. [71].

The tracking of a charged particle was performed with a cylindrical drift chamber (CDC) and a barrel-shaped drift chamber (BDC). A vertex drift chamber (VTC) was also installed around the nuclear targets to improve the position resolution of vertex. In this analysis, however, we do not use the VTC information, because the mass acceptance of the VTC is significantly different between the nuclear targets. These tracking devices were arranged inside a magnetic field provided by the dipole magnet. The strength of the field was 0.71 T at the center of the magnet. The integrated field over the interval between the center of the magnet to the outer most tracking device (BDC) was 0.81 T·m.

Electron identification was performed with a combination of electron identification counters. They were divided into three stages. The first stage counter was front gas Cherenkov counters (FGC) covering from $\pm 12^\circ$ to $\pm 90^\circ$ horizontally and $\pm 23^\circ$ vertically. The second stage counters consisted of three types of counters: rear gas Cherenkov counters (RGC), rear lead-glass calorimeters (RLG), and side lead-glass calorimeters (SLG). Figure 2.3 shows the acceptance of the second stage counters. The RGC covered from $\pm 12^\circ$ to $\pm 54^\circ$ horizontally and $\pm 6^\circ$ vertically. The RLG covered from $\pm 12^\circ$ to $\pm 54^\circ$ horizontally and from $\pm 9^\circ$ to $\pm 23^\circ$ vertically. The SLG covered from $\pm 57^\circ$ to $\pm 90^\circ$ horizontally and $\pm 23^\circ$ vertically. These three counters of the second stage together cover nearly the same acceptance of the first stage. The third stage counter was forward lead-glass calorimeters (FLG) covering from 12° to 54° in the left arm and -12° to -40° in the right arm, horizontally and $\pm 7^\circ$ vertically. The angular coverage of the third stage was limited to forward region and smaller compared to those of the first and second stages. Depending on the particle trajectories, two or three stages were used to identify electrons and positrons.

Start timing counters (STC) provide the time zero for an event. It was used to measure the drift time in the drift chambers, and the time-of-flight at the above-mentioned Cherenkov counters and lead-glass calorimeters. The STCs were placed around the inner ridge of the CDC at 380 mm from the nuclear targets. The STCs were used because we did not count beam protons particle by particle due to the high intensity of the beam.

Kaon identification capability was provided by the following counters, which were not used in this thesis: Aerogel Cherenkov counters (AC), forward time of flight counters (FTOF), and hodoscope counters (HD).

The acceptance of each detector relevant to this analysis is summarized in Table 2.1. In the following sections, details of each detector are described.

2.2 Accelerator facility and beamline

The proton synchrotron facility at KEK consists of four stages of accelerators, the 750 kV Cockroft-Walton, the 40 MeV linear particle accelerator, the 500 MeV

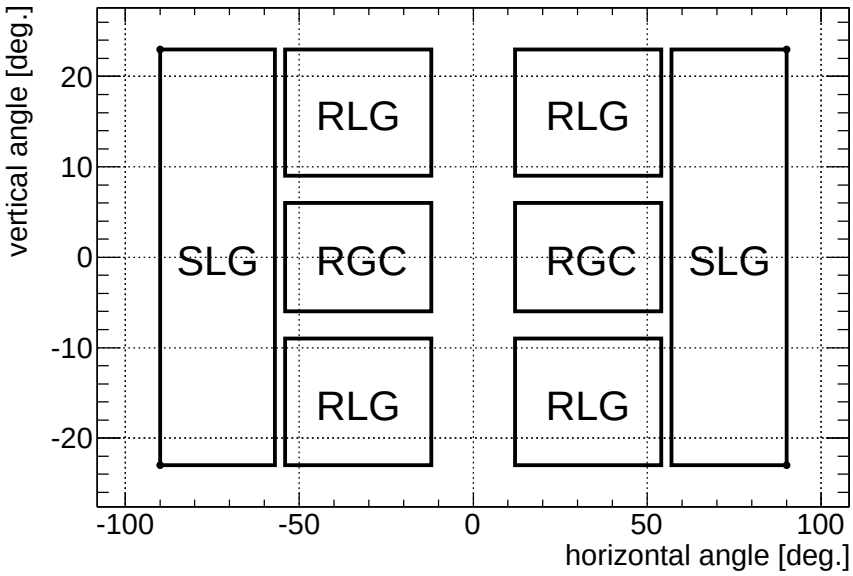

Figure 2.3: Acceptance of the electron identification counters of second stage.

Table 2.1: Acceptance of the detectors in the left arm. The right arm covers the symmetrical acceptance with respect to the beam axis.

	horizontal acceptance [degree]	vertical acceptance [degree]
CDC	12–132	−22 to 22
BDC	7.5–94.5	−22 to 22
FGC	12–90	−23 to 23
RGC	12–54	−6 to 6
RLG	12–54	−23 to −9, 9–23
SLG	57–90	−23 to 23
FLG	12–54 (−40 to −12)*	−7 to 7

* left arm (right arm)

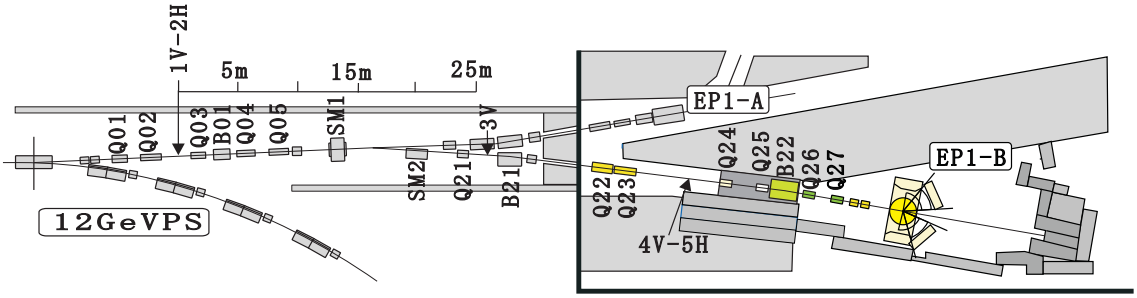

Figure 2.4: Schematic view of Beam Line (EP1-B). Taken from Fig. 2.4 in Ref. [74].

booster synchrotron, and the 12 GeV PS.

The typical beam intensity was 3×10^{12} protons per spill in PS. When our experiment was conducted, the beam were delivered to two primary beamlines simultaneously: approximately 1% to the EP1 beamline and approximately 99% to the EP2 beamline. The beam transported to the EP1 can be switched either to EP1-A or to EP1-B. The EP1-A line was used for the production of secondary particles in the slow extraction mode and for the neutrino oscillation experiment (K2K) in the fast extraction mode. The EP1-B line was a special beamline to use primary protons. This experiment was conducted at the EP1-B line. The schematic view of the EP1-B line is shown in Fig. 2.4.

When the EP1-B line is in operation, protons from the PS were delivered to the EP1 line and were focused to a set of collimators 1V and 2H with a set of quadrupole magnets Q01 and Q02. The initial image of the beam was defined by the vertical collimator 1V and the horizontal collimator 2H. At these collimators, the image of the beam was vertically long so that the beam intensity was controlled by changing the aperture of the vertical collimator 1V. The vertical collimator 1V typically reduced the beam intensity to one-fifteenth. Typical aperture of the collimators 1V and 2H were 8.0 mm and 2.2 mm, respectively. The beam was bent by six degrees with two steering magnets SM1 and SM2, and was vertically focused to a vertical collimator 3V with a set of quadrupole magnets Q03, Q04, Q05, and Q21. The vertical collimator 3V reduced the beam halo. Then the beam was transported to the first focal point at collimators 4V and 5H with a 'DQQ' (B21, Q22, Q23) complex. The collimators 4V and 5H reduced the beam halo again. After the other beam-focusing complex 'QQDQQ' (Q24, Q25, B22, Q26, Q27), the beam was transported to the final focal point at the center of the spectrometer. The spot size at the targets was 1–2 mm in full width at half maximum. The beam intensity was monitored with an ionization chamber with an accuracy of 10% at the downstream of the spectrometer [75]. The repetition period was four seconds, and the flat top

Table 2.2: Setting of the collimator width.

year	1V	2H	3V	4V	5H
2001	8.0 mm	4.0 mm	50 mm	*full*	15.0 mm
2002		2.7 mm	*full*		

of a spill was approximately 1.8 seconds.

The aperture of the collimators were tuned to reduce trigger requests due to a beam halo. The collimator settings in data-taking periods for this analysis are shown in Table 2.2. The collimator 4V in 2001 and the collimators 3V and 4V in 2002 were fully opened, because these collimators were not effective to reduce a beam halo. The field strength of the magnets B21 and B22 were also tuned to reduce a beam halo. The interaction rate of a beam halo with beam pipes was minimized by controlling the beam trajectory. The setting was determined by scanning the field strength as trigger requests became minimum. This tuning was performed in every accelerator tuning cycle of approximately two weeks. The extraction status of the beam changed in every cycle, while it was quite stable within a cycle.

2.3 Spectrometer magnet

The spectrometer magnet was a dipole magnet with a weight of 300 ton, a length of 2120 mm, a width of 5655 mm, and a height of 3980 mm. The schematic view of the magnet is shown in Fig. 2.5. Both pole pieces of the magnet consisted of two layers of cylindrical shaped iron with a diameter of 1760 mm and 2120 mm, which ensured a maximum vertical acceptance of ± 22 degrees for electrons. The gap between the pole pieces was 907 mm.

The magnetic field at the center of the pole piece was tuned to 0.71 T, resulting in the integrated magnetic field $\int B \cdot dl$ of 0.81 T·m from the targets to the BDC at 1680 mm from the targets.

A magnetic field map in the acceptance was obtained with a calculation. The field calculation was performed using TOSCA [76] which used the finite element method. The field measurement was also performed using a Hall-probe in a part of the whole region to estimate a systematic uncertainty of the magnetic field map. The systematic uncertainty of the momentum due to the systematic uncertainty of the magnetic field map was evaluated. Drift chamber hits along the trajectory of a charged particle were generated based on the measured magnetic field, and the hits were fitted with the Runge–Kutta method based on the calculated magnetic field map. The discrepancy between an original momentum and a reconstructed

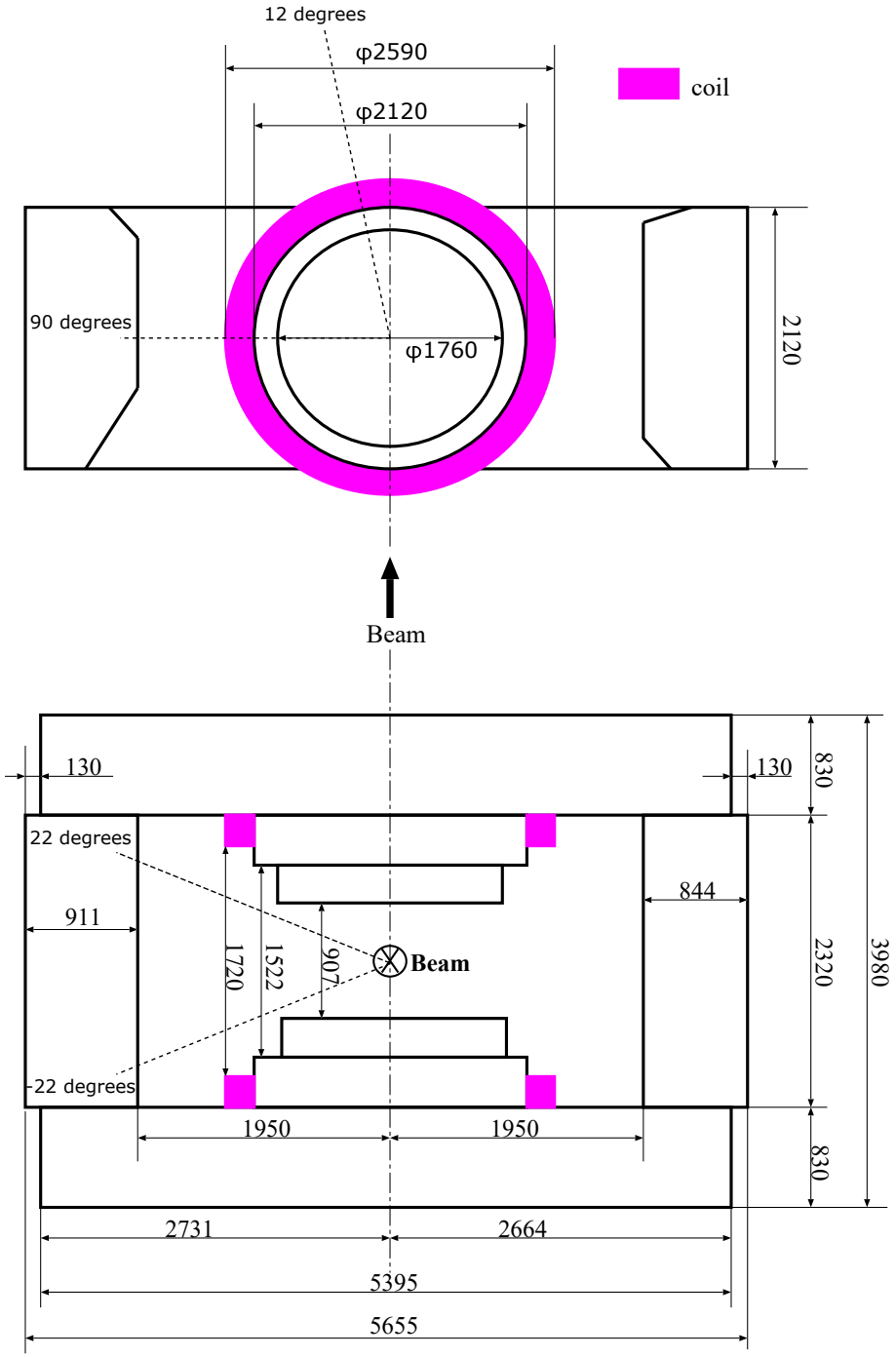

Figure 2.5: Schematic view of the spectrometer magnet. The dashed lines represent the acceptance for electrons. Based on Fig. 3 in Ref. [71].

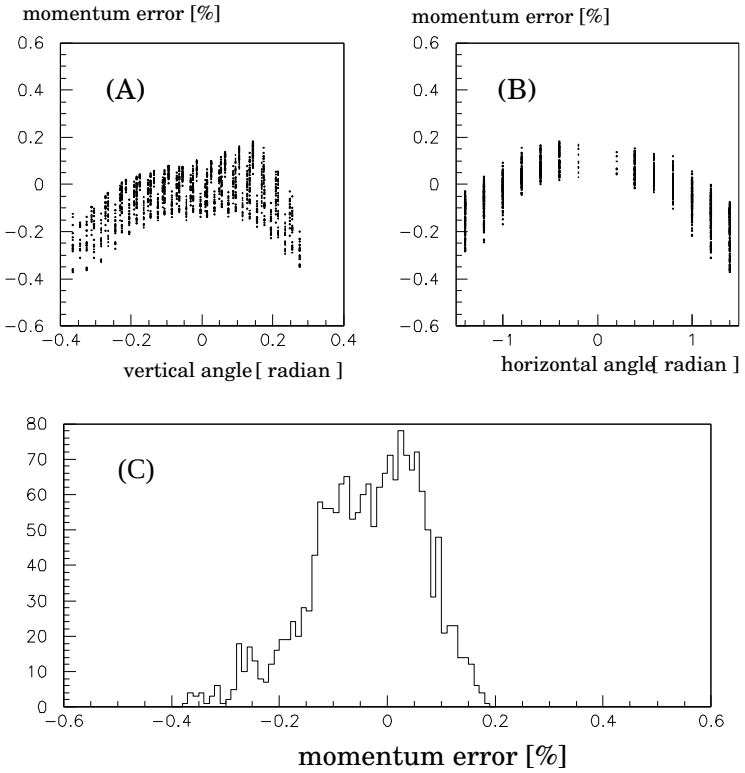

Figure 2.6: Uncertainty of the momentum due to inaccuracy of the magnetic field map. A) The difference of an original momentum and a reconstructed momentum as a function of the vertical angle. B) The difference of an original momentum and a reconstructed momentum as a function of the horizontal angle. C) The projection of all the differences. Taken from Fig. 2.9 in Ref. [74].

momentum was within $0.2\% \pm 0.3\%$ in the momentum region 0.5 to 2.0 GeV/c. The nominal discrepancy of 0.2% was corrected by scaling the field map. Figure 2.6 shows the discrepancy between an original momentum and a reconstructed momentum after the correction.

Run by run correction of the field map was also performed. The magnetic field at the center of the magnet was monitored with a nuclear magnetic resonance probe at the beginning and the end of each run. The averaged value was used for each run as a scaling factor of the field map. Typical variations of the scaling factors was as small as 0.07%.

Table 2.3: Size, interaction length, and radiation length of each target. A star represents the value is the same as that in 2001.

year	material	atomic weight	width [mm]	height [mm]	thickness [g/cm^2]	interaction length [%]	radiation length [%]
2001	C	12.011 [77]	25	25	0.092	0.106	0.215
	Cu	63.546 [77]	25	25	0.073	0.054	0.565
2002	C	$\star$	10	25	0.184	0.213	0.431
	Cu	$\star$	10	25	0.073	0.054	0.565

2.4 Targets

As nuclear targets, carbon and copper targets were used. In 2001, one carbon target and two copper targets were installed in the spectrometer. In 2002, one carbon target and four copper targets were installed. These target were aligned in the beam line as the beam penetrated all the targets. From the upstream to the downstream, the name of each target was defined as Cu-1, C, and Cu-2 in 2001, and Cu-1, Cu-2, C, Cu-4, and Cu-5 in 2002. The size, interaction length, and radiation length of each target are summarized in Table 2.3. Each target was so thin that the conversion probability of two γ's from a π^0 inside each target is smaller than the branching ratio of the π^0 Dalitz decay, which is 1.2%.

Each target was installed at the center of the CDC and attached on a polyethylene stay with a thickness of 1 mm. The space between each target was designed to be 46 mm and 23 mm in 2001 and 2002, respectively. The width of each target was so narrow that no other targets were in the acceptance of itself.

2.5 Beam profile

The beam profile at the target position was measured with the carbon target. The carbon target was able to be rotated by 90 degrees around the z-axis. The rotated carbon target worked as a probe with a width of 0.5 mm and 1.0 mm in 2001 and 2002, respectively. We counted the interaction rate as we moved the beam position horizontally by changing the voltage of the bending magnet B22 located at the most downstream of the EP1-B line (Fig. 2.4). The interaction rate as a function of the position of the horizontal beam center is shown in Fig. 2.7. Assuming that the beam profile of the horizontal direction followed a Gaussian distribution, the data were fitted with a rectangle profile of the carbon target convoluted with a Gaussian distribution. The one standard deviation of the horizontal beam size was evaluated

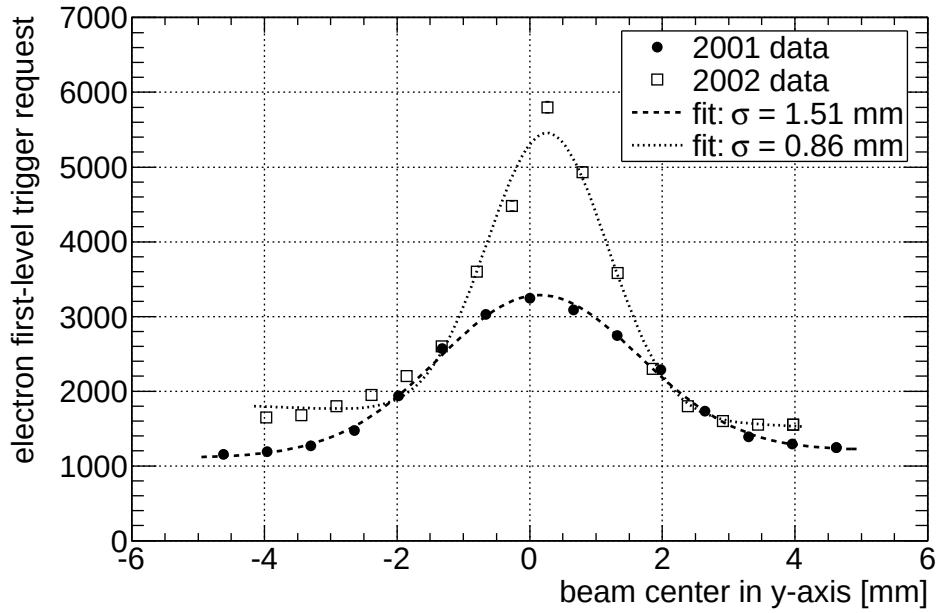

Figure 2.7: Interaction rate as a function of the horizontal beam position. The solid symbols and the open symbols represent the data in 2001 and 2002, respectively. The dashed line and the dotted line represent the fit result of 2001 data and of 2002 data, respectively.

to be 1.51 mm and 0.86 mm in 2001 and 2002, respectively.

2.6 Tracking chambers

Tracking of a charged particle was performed with two types of drift chambers: a cylindrical drift chamber (CDC) and barrel-shaped drift chamber (BDC). This section describes mechanical design of the CDC and the BDC and the momentum resolution.

2.6.1 Cylindrical drift chamber (CDC)

The CDC, installed on a pole piece of the spectrometer magnet, worked as the inner most tracking device for this analysis. The shape of the CDC was a hollow cylinder with an inner diameter of 800 mm, an outer diameter of 1760 mm, and a height of 840 mm, as shown in Fig. 2.8. The acceptance of the CDC was from ±12 degrees to ±132 degrees horizontally and ±22 degrees vertically.

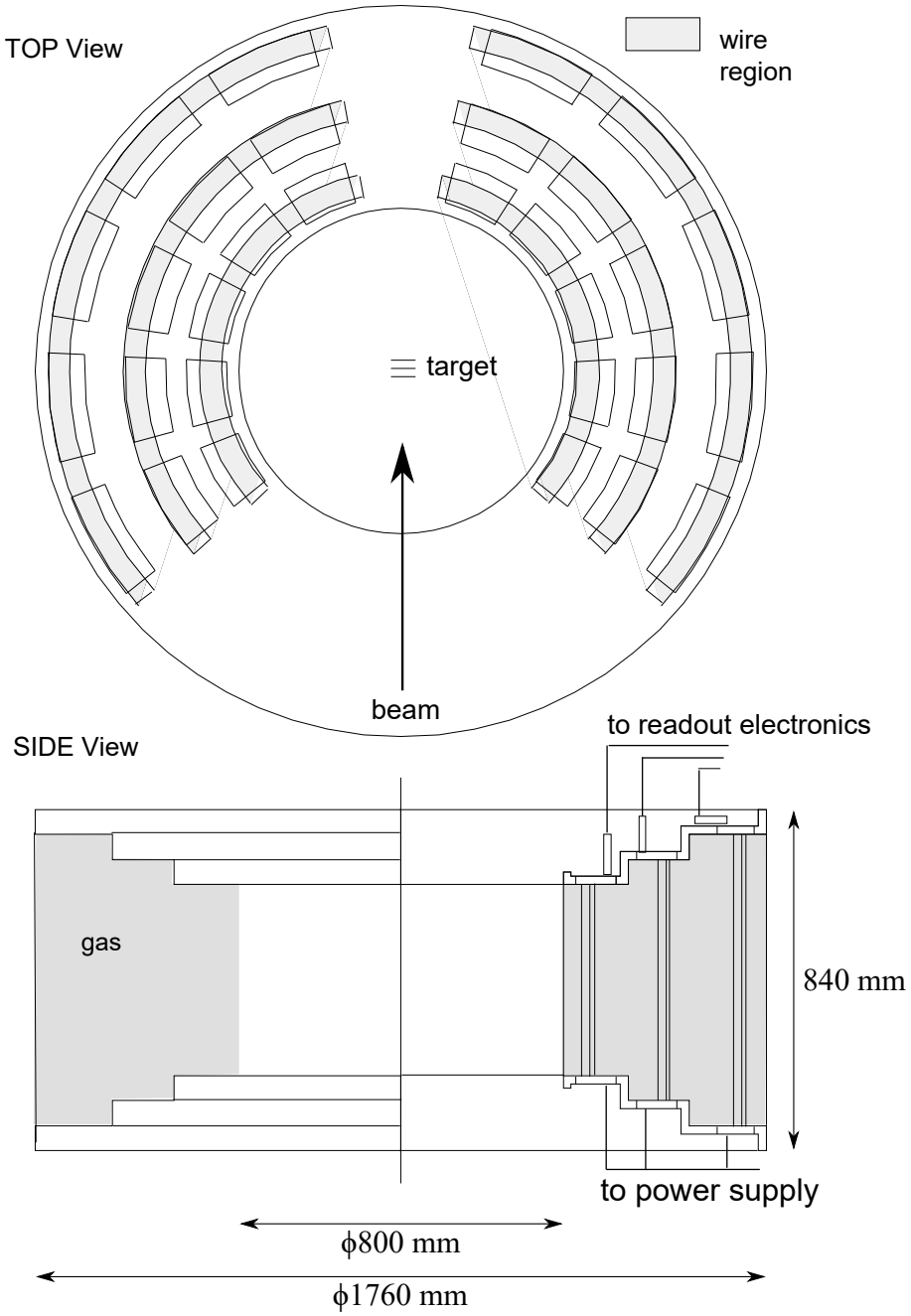

Figure 2.8: Schematic view of the CDC. The CDC covers from a diameter of 800 mm to 1760 mm with a height of 840 mm. Based on Fig. 4 in Ref. [71].

Table 2.4: Wire arrangement of the CDC

super-layer	inner			middle				outer		
radial layer ID	1	2	3	4	5	6	7	8	9	10
wire direction	X	X′	U	V	V′	X	X′	U	X	X′
radial location of sense wires [mm]	445	455	475	602.5	612.5	632.5	642.5	800	820	830
cell width [degree]	1.5	1.5	1.5	1.5	1.5	1.5	1.5	1.5	1.5	1.5
cell width [mm]	11.65	11.91	12.43	15.77	160.4	16.55	16.82	20.94	21.47	21.73
tilt angle [rad]	0	0	−0.11	0.11	0.11	0	0	−0.12	0	0
wire length [mm]	441	441	443.8	568.5	568.7	565	565	717.9	713	713
number of sense wires	81	81	77	76/77*	77/76*	81	81	77	82	82

* left arm/right arm

The CDC had three super-layers, and each super-layer consisted of three or four radial layers. A wire configuration is shown in Fig. 2.9. The inner super-layer had three radial layers (X, X′, and U) on a radius of 445 mm, 455 mm, and 475 mm, respectively. The middle super-layer had four radial layers (V, V′, X, and X′) on a radius of 602.5 mm, 612.5 mm, 632.5 mm, and 642.5 mm, respectively. The outer super-layer had three radial layers (U, X, and X′) on a radius of 800 mm, 820 mm, and 830 mm, respectively. The wire direction of X and X′ were parallel to the z-axis, that is, the magnetic field, while that of U, V, and V′ were tilted by approximately −0.1 radians, 0.1 radians, and 0.1 radians, respectively. The width of each drift cell was 1.5 degrees with respect to the center of the CDC. Argon-ethane mixed gas of 50% and 50% at 1 atm flowed as a working gas at a rate of 100 ml/min. A typical hit rate in the inner super-layer is approximately 60 kHz/wire.

Each sense wire was a gold-plated tungsten wire of 30 µm diameter, while each potential wire was a Be-Cu wire of 100 µm diameter. Each wire was fixed on the chamber via a bush inserted at the end of a feed-through pipe. The bush used for a sense wire had a hole with a diameter of 80 µm, so that the position accuracy of the sense wires were 25 µm. The high voltage of −1.37 kV and −2.1 kV were applied to guard wires and potential wires in the inner super-layer, respectively. For the middle super-layer and the outer super-layer, the high voltage of −1.43 kV and −2.2 kV were applied to guard wires and potential wires, respectively. All sense wires were kept at the ground level. Details of a wire arrangement are shown in Table 2.4.

Read-out electronics of the CDC consisted of an integrated circuits (IC) of Amplifier-Shaper-Discriminator (ASD), a LVDS-ECL converters, and a time to digital converters (TDC). The ASD IC was developed for the thin gap chamber in the forward muon trigger system of the LHC ATLAS experiment [78]. The measured gain of a pre-amplifier of each ASD was 360 mV/pC, and that of a main amplifier

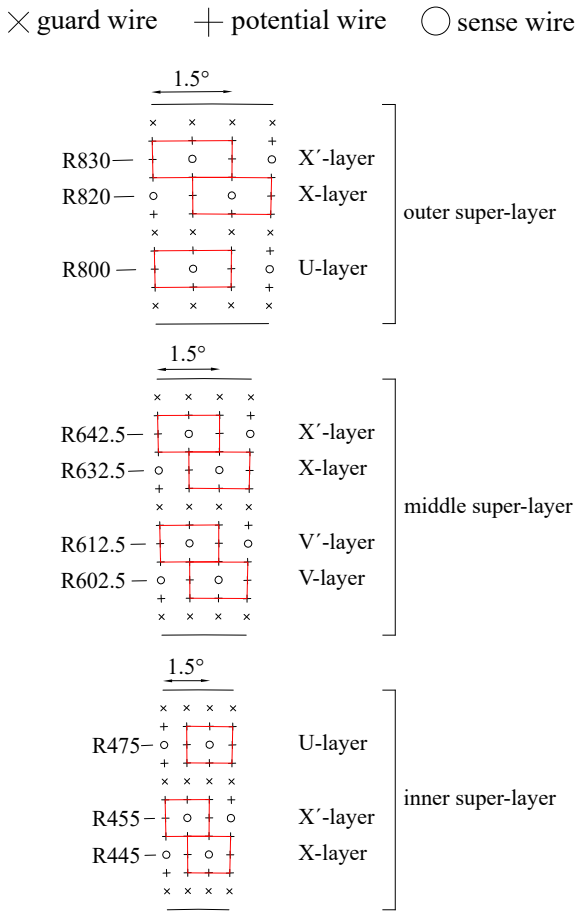

Figure 2.9: Cell structure of the CDC. Ten radial layers, grouped into three super-layers, compose the CDC.

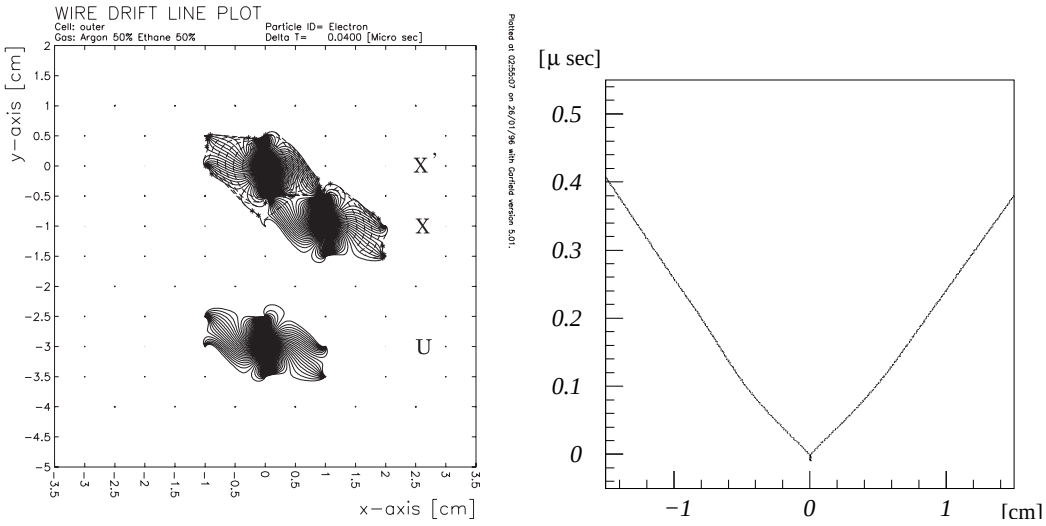

(a) (b)

Figure 2.10: (a) Drift lines in the outer super-layer. (b) Calculated relation between the drift time and the drift length of the X layer. Taken from Fig. 2.17 in Ref. [74].

was four. The output signal of each ASD was transferred to a LVDS-ECL converter via a twisted-pair cable with a length of 10 m. The output signal of a LVDS-ECL converter was transferred to a TDC at the counting house via a twisted-pair cable with a length of 35 m.

When a minimum ionizing particle passed through a drift cell of the CDC, it produced approximately 100 ionization electrons. These ionization electrons were amplified by a factor of 1.6×10^4 due to an electron avalanche took place around a sense wire. The measured pulse height before a discriminator was typically 240 mV for a minimum ionizing particle. The threshold voltage on a pulse height for the discriminator was from 5 to 18 mV, depending on a super-layer of the CDC.

The configuration of an electric field in each drift cell and the relation between the drift length and the drift time (x-t relation) was firstly evaluated with the drift chamber simulation code Garfield [79]. The drift lines of ionization electrons in each layer were calculated with the simulation and that in the outer super-layer is shown in Fig. 2.10(a). Based on this simulation, the x-t relation is obtained as the systematic shifts in a residual distribution between a hit point and a track position by the Runge–Kutta fitting as a function of the drift length gets minimum. Figure 2.10(b) shows the obtained x-t relation in the X layer.

Table 2.5: Wire arrangements of the BDC

layer ID	1	2	3	4
wire direction	X	X′	U	V
location of sense wires [mm]	1600	1610	1630	1650
cell width [degree]	0.75	0.75	0.75	0.75
cell width [mm]	20.81	20.94	21.21	21.47
tilt angle [rad]	0	0	−0.11	0.11
wire length [mm]	1403	1403	1410.9	1411.1
number of sense wires	116	116	109	109

2.6.2 Barrel-shaped drift chamber (BDC)

The BDC was installed right behind the FGC and worked as the outer most tracking device for this analysis. The shape of the BDC was a hollow cylinder with an inner diameter of 1570 mm, an outer diameter of 1680 mm, and a height of 1420 mm, as shown in Fig. 2.11. The BDC covers from ±7.5 degrees to ±94.5 degrees horizontally and ±22 degrees vertically. The vertical acceptance of the BDC is the same as that of the CDC.

The BDC had four layers (X, X′, U, V) on radii of 1600 mm, 1610 mm, 1630 mm, and 1650 mm. A wire configuration is shown in Fig. 2.12. The wire direction of X and X′ were parallel to the z-axis, that is, the magnetic field, while that of U and V were tilted by approximately 0.1 radians and −0.1 radians, respectively. The width of each drift cell was 0.75 degrees with respect to the center of the BDC. The size of a drift cell of the BDC was the same as that of the outer super-layer of the CDC. Argon-ethane mixed gas of 50% and 50% at 1 atm flowed as a working gas at a rate of 100 ml/min.

Each sense wire was a gold-plated tungsten wire of 30 µm diameter and each potential wire was a Be-Cu wire of 100 µm diameter as the CDC. The high voltage of 0.1 kV, −0.7 kV, and 1.5 kV were applied to guard wires, potential wires, and sense wires, respectively. Details of a wire arrangement are shown in Table 2.5.

Read-out electronics of the BDC was the same as that of the CDC. The threshold voltage on a pulse height for a discriminator was from 13 to 15 mV.

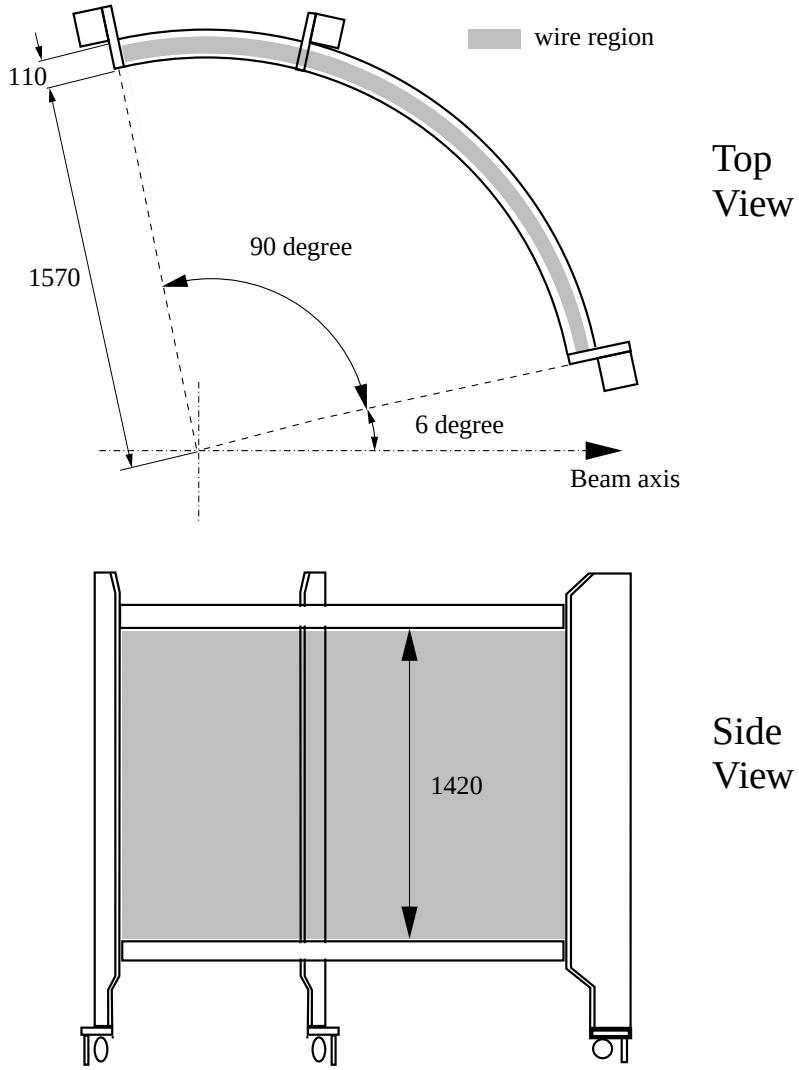

Figure 2.11: Schematic view of the BDC. The BDC covers from a diameter of 1570 mm to 1680 mm with a height of 1420 mm. Taken from Fig. 6 in Ref. [71].

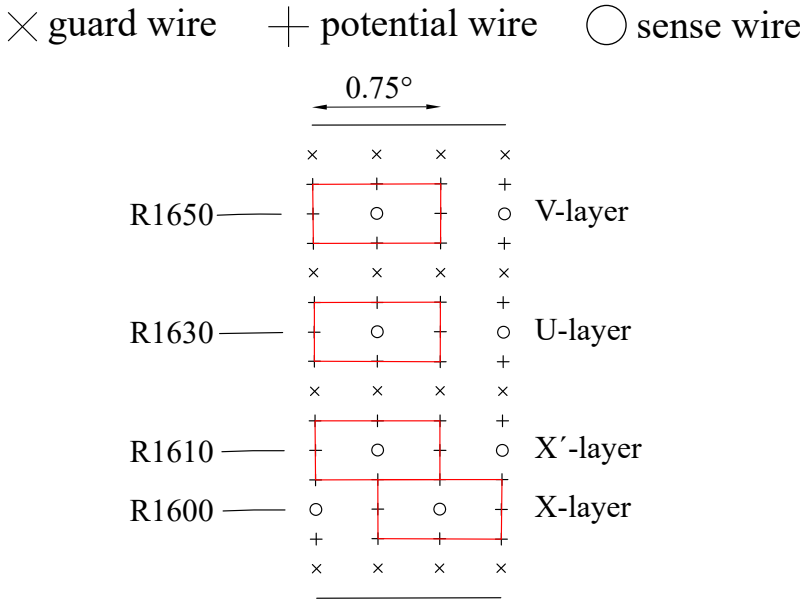

Figure 2.12: Cell structure of the BDC. Four layers compose the BDC.

2.6.3 Material budget of the tracking devices

The material budget from the targets to the outer most tracking device of the BDC is summarized in Table 2.6. The momentum resolution of the whole tracking system was evaluated with a GEANT4 [80] based detector simulation including experimental effects and position resolution of the CDC and the BDC. The detail is described in Sec. 3.8.5.

2.7 Start timing counter (STC)

The STC defined the time zero of an event. The STC was installed along an arc with a radius of 380 mm, covering from ±12 degrees to ±60 degrees horizontally, and ±23 degrees vertically. The STC was segmented into eight segments in each arm. The schematic view of a segment is shown in Fig. 2.13.

Each Segment consisted of a scintillator, two light guides, two 2-inch fine-mesh photo-multipliers (PMT), and two sets of aluminum jigs. The scintillator was made of Bicron BC404 with a width of 40 mm, a height of 400 mm, and a thickness of 5 mm. At both ends of each segment, the PMTs were attached to the light guides with optical grease. The PMT was H6154 of Hamamatsu Photonics, which had a 2-inch diameter photocathode and fine-mesh dynodes. Because of the fine-mesh structure, the typical gain of the PMT was 1×10^6 even under the magnetic field

Table 2.6: List of the materials and their radiation lengths from the targets to the BDC.

counter	material	radius [mm]	thickness X [mm]	λ_{rad} [mm]	X/λ_{rad} [%]
VTC	Ar-C_2H_6 (50:50)	0.00	245.00	340350.0	0.072
	Wire (Cu-Be)	-	0.0173	14.3	0.121
	Wire (W)	-	0.0004	3.5	0.011
	Mylar	245.00	0.05	287.0	0.017
	air	245.05	134.95	304200.0	0.044
STC	scintillator	380.00	5.00	425.0	1.176
	lapping	385.00	0.20	287.0	0.070
	air	385.20	14.80	304200.0	0.005
CDC	Mylar	400.00	0.05	287.0	0.017
	Ar-C_2H_6 (50:50)	400.05	479.95	340350.0	0.141
	Wire (Cu-Be)	-	0.031	14.3	0.217
	Wire (W)	-	0.0005	3.5	0.014
	Mylar	880.00	0.05	287.0	0.017
	air	880.05	19.90	304200.0	0.007
FGC	Mylar	899.95	0.05	287.0	0.017
	isobutane	900.00	660.00	169300.0	0.390
	acrylic mirror	1560.00	3.00	344.0	0.872
	aluminum cover	1563.00	1.00	89.0	1.124
	air	1564.00	5.95	304200.0	0.002
BDC	Mylar	1569.95	0.05	287.0	0.017
	Ar-C_2H_6 (50:50)	1570.00	110.00	340350.0	0.032
	Wire (Cu-Be)	-	0.010	14.3	0.070
	Wire (W)	-	0.0001	3.5	0.003
total					4.458

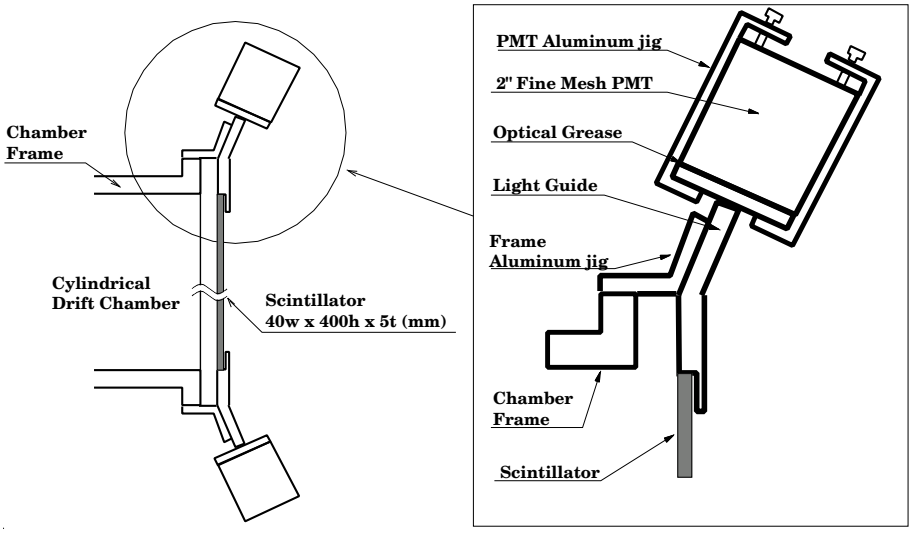

Figure 2.13: Schematic view of an STC segment. Taken from Fig. 2.25 in Ref. [81].

of 0.71 T at the STC position. The scintillation light produced in the scintillator propagated via the light guides into the PMTs. The coincidence rate of the top and the bottom PMTs was approximately 1 MHz on spill at the most forward segments close to the beam, thus an additional circuit was added to the voltage divider for providing enough current to the last three dynodes. Typically, the voltage divider current was 0.4 mA and the current of the additional circuit was 4 mA. Signals from the top and the bottom PMT were discriminated and then were transferred to a mean timer which determined the timing of each segment. The difference of the timing between each segment was tuned within 1 ns. These Signals were OR-ed and were used as the event time-zero signal. The time resolution of the STC is approximately 0.3 nsec.

2.8 Electron identification counters

The electron and positron identification was performed with two or three stages of electron identification counters. The first stage was front gas Cherenkov counters (FGC). The second stage consisted of three types of counters: rear gas Cherenkov counters (RGC), rear lead-glass calorimeters (RLG), and side lead-glass calorimeters (SLG). The third stage was forward lead-glass calorimeters (FLG). This section describes mechanical design of the FGC, the RGC, the RLG, the SLG, and the FLG.

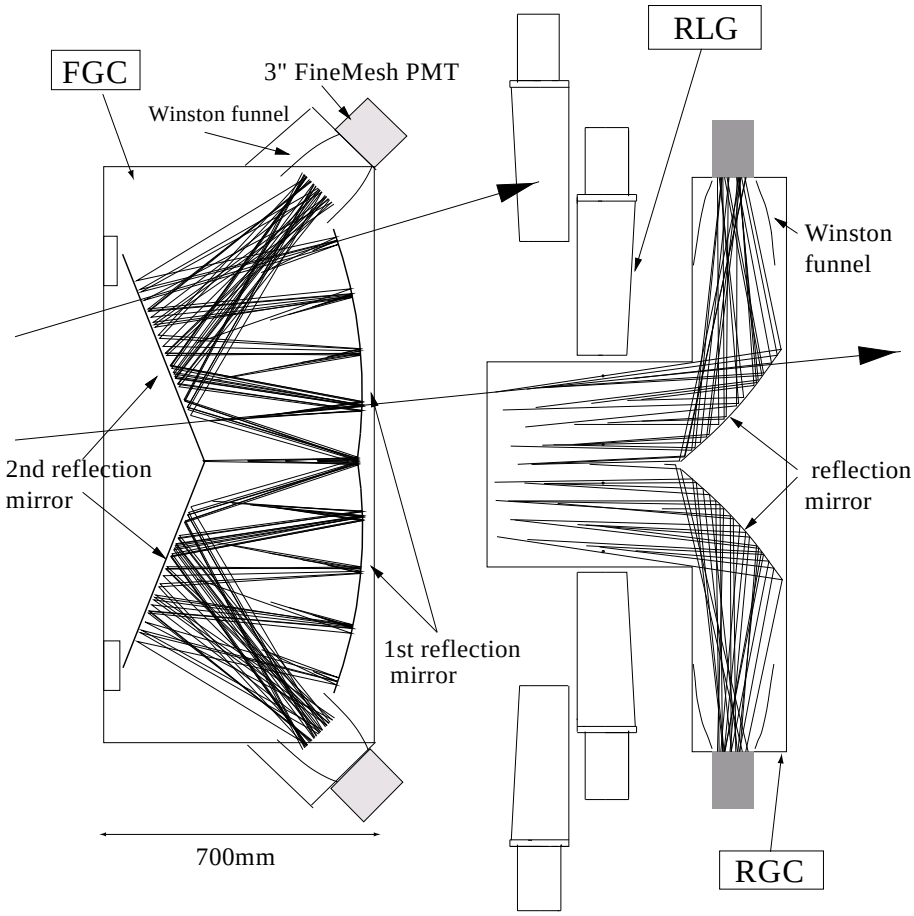

Figure 2.14: Schematic view of the FGC, the RGC, and the RLG with a light collection scheme. Based on Fig. 11 in Ref. [71].

2.8.1 Front gas Cherenkov counter (FGC)

The FGC was used for electron identification of the first stage. The FGC was installed between the CDC and the BDC. The FGC covered from ±12 degrees to ±90 degrees horizontally, and ±23 degrees vertically, which was the full acceptance of the electron identification for this spectrometer. The FGC was horizontally segmented into 13 segments in each arm, resulting in horizontal acceptance of six degrees per segment. The schematic view of the FGC is shown in Fig. 2.14, together with a light collection scheme.

Each segment consisted of an iso-butane gas radiator, three types of mirrors, and two PMTs. The refractive index of iso-butane is 1.00127 at room temperature and 1.0019 at 0°C, which corresponds to the threshold momentum for a pion of

2.7 GeV/c and 2.3 GeV/c, respectively. The FGC was operated at approximately 15°C. There were two reasons why the iso-butane gas radiator with rather high refractive index was used. Firstly, the path length of a particle in the FGC was short, thus the high refractive index is necessary for the enough Cherenkov photon yield. Secondly, iso-butane gas shows high transparency for ultra-violet (UV) light down to the wavelength of 220 nm. The shorter wavelength was important to detect more Cherenkov photons, because the yield of the Cherenkov light had the dependence of $1/\lambda^2$.

An incident electron emitted Cherenkov photons in the radiator. An emitted Cherenkov photon was reflected twice by a flat mirror and an arc-shaped mirror and was focused into a PMT with a Winston funnel [82]. The mirrors were thin to avoid the unnecessary multiple scattering. The flat mirror was a 0.05 mm-thick aluminized Mylar supported by a honeycomb backplane made of paper. The arc-shaped mirror was a 3 mm-thick acrylic plastic with aluminum and SiO evaporated on it. The other mirrors were at the both sides of a segment, which also worked as partitions to the next segments. The side mirror was MgF_2-coated aluminized Mylar with 88% reflectance for the wavelength down to 200 nm. A reflected Cherenkov photon was focused into a 3-inch PMT with a Winston funnel attached to the PMT. The funnel was an acrylic plastic with aluminum and SiO evaporated on it. The PMT was R5542 of Hamamatsu Photonics, which had a 3-inch diameter photocathode and 19 fine-mesh dynodes. Because of the fine-mesh structure, this PMT was able to be used for the FGC even under the magnetic field of 0.2 T at the FGC position.

With a beam test, the pion rejection is found to be 0.8×10^{-2} for a pion at 1 GeV/c when a threshold is set to one photoelectron.

2.8.2 Rear gas Cherenkov counter (RGC)

The RGC was used for electron identification of a part of the second stage: the RGC, the RLG, and the SLG. The RGC was installed behind the BDC. The RGC covered from ±12 degrees to ±54 degrees horizontally, and ±6 degrees vertically. The RGC was horizontally segmented into seven segments in each arm, resulting in horizontal acceptance of six degrees per segment. The schematic view of the RGC is shown in Fig. 2.14, together with a light collection scheme.

Each segment consisted of an iso-butane gas radiator, two types of mirrors, and two PMTs. Iso-butane gas was the same as the FGC.

An incident electron emitted Cherenkov photons in the radiator. A emitted Cherenkov photon was reflected by an arc-shaped mirror and was focused into a PMT with a Winston funnel. The arc-shaped mirror was a 3 mm-thick acrylic plastic with aluminum and SiO evaporated on it. The other mirrors were placed at the both sides of a segment, which also worked as partitions to the next segments. A

reflected Cherenkov photon was focused into a 3-inch PMT with a Winston funnel attached to the PMT. The PMT was R1652 of Hamamatsu Photonics, which had a 3-inch diameter photocathode.

With a beam test, the pion rejection is found to be 3×10^{-3} for a pion at 1 GeV/c when the electron identification efficiency of 99% is required.

2.8.3 Rear lead-glass electromagnetic calorimeter (RLG)

The RLG was used for electron identification of a part of the second stage: the RGC, the RLG, and the SLG. The RLG was installed to cover the same angle horizontally as the RGC did, but to cover regions above and below the RGC acceptance. The RLG covered from ±12 degrees to ±54 degrees horizontally, which was the same as the RGC, and from ±9 degrees to ±23 degrees vertically. The RLG consisted of eight units and each unit had 12 segments, which lined horizontally. The schematic view of the RLG is shown in Fig. 2.14. Two units were located both above and below the RGC, resulting in four units in each arm. The two units were vertically staggered to cover a larger acceptance.

Each segment consisted of a PMT and a SF6W lead-glass block with a width of 124 mm, a height of 340 mm, and a thickness of 114 mm. The PMT was R1652 of Hamamatsu Photonics, which had a 3-inch diameter photocathode. The material properties of SF6W are shown in Table 2.7. The lead-glass blocks were recycled from the barrel electromagnetic calorimeter of the TOPAZ experiment at TRISTAN, KEK [83].

An incident particle come into the side of a lead-glass block, as shown in Fig. 2.14. Thus, an effective thickness as a Cherenkov radiator was 6.7 radiation length. Cherenkov photons emitted from an electromagnetic shower were propagated into a PMT at the end of a block via the reflections on the surface of the block. The typical energy resolution was $\sigma_E/E \sim 18\%$ for an electron at 1 GeV/c.

2.8.4 Side lead-glass electromagnetic calorimeter (SLG)

The SLG was used for electron identification of a part of the second stage: the RGC, the RLG, and the SLG. The SLG was installed behind the BDC along the return yokes of the magnet to cover the backward region. The SLG covered from ±57 degrees to ±90 degrees horizontally, and ±23 degrees vertically. The SLG was horizontally segmented into nine segments in each arm. The schematic view of the SLG is shown in Fig. 2.15.

Each segment consisted of five SF6W lead-glass blocks and two PMTs. The lead-glass blocks were recycled from the barrel electromagnetic calorimeter of the TOPAZ experiment at TRISTAN, KEK as the RLG. Each lead-glass block was re-polished and reshaped into a rectangular shape with a width of 120 mm, a height

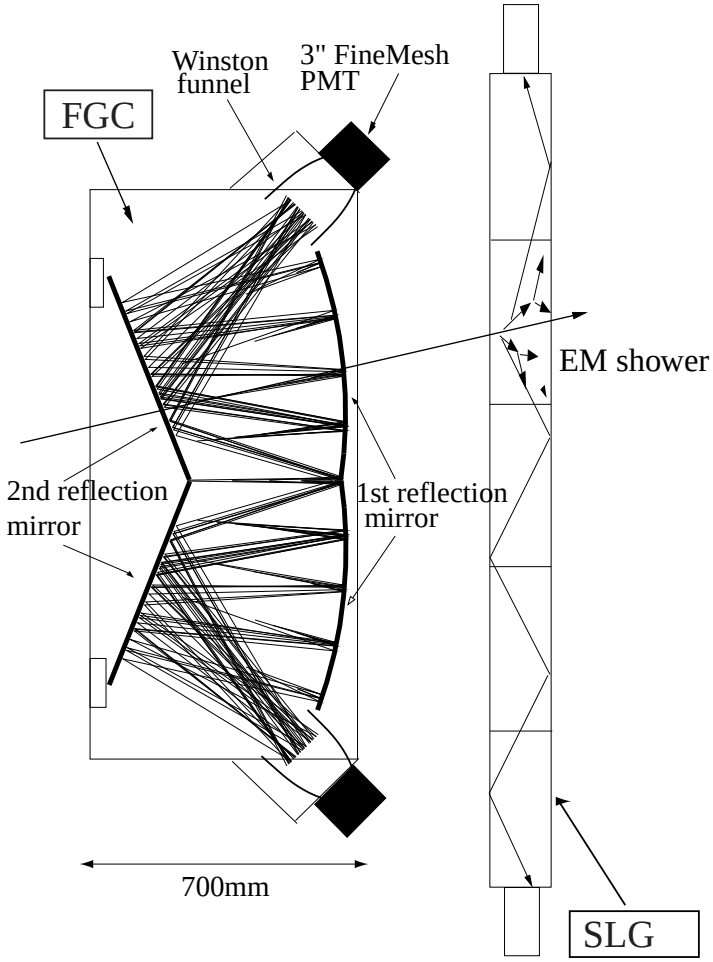

Figure 2.15: Schematic view of the FGC and the SLG. Based on Fig. 13 in Ref. [71].

Table 2.7: Chemical composition and physical properties of SF6W [83].

chemical composition (wt%)	
SiO_2	27.3
PbO	70.9
K_2O	0.9
Na_2O	0.6
Sb_2O_2	0.3
radiation length [cm]	1.69
refractive index	1.805
density [g/cm^3]	5.20
critical energy [MeV]	12.6
Molière radius [cm]	2.8

of 330 mm, and a thickness of 110 mm from the original tapered shape. Five lead-glass blocks were stacked vertically and were glued together, resulting in the size of 120 mm in width, and 1650 mm in height, and 110 mm in thickness. At each end of the lead-glass blocks, the PMT of R1911 of Hamamatsu Photonics, which had a 3-inch diameter photocathode, was installed.

An incident particle came into the side of a lead-glass block, as shown in Fig. 2.15. Thus, an effective thickness as a Cherenkov radiator was 6.5 radiation length. Cherenkov photons emitted from an electromagnetic shower were propagated into the PMT at the end of a block via the reflections on the surface of the block. The typical energy resolution was $\sigma_E/E \sim 20\%$ for an electron at 1 GeV/c.

2.8.5 Forward lead-glass electromagnetic calorimeter (FLG)

The FLG was installed at the outer most region of the spectrometer and was intended to have the same acceptance as the RGC of the second stage did. However, the FLG of the right arm had smaller horizontal acceptance compared to the RGC, due to the space limitation of the experimental area. The horizontal acceptance of the FLG covered from 12 degrees to 54 degrees in the left arm, which is the same as the RGC, and from -12 degrees to -40 degrees in the right arm. The FLG covered from ± 7 degrees vertically. The FLG was horizontally segmented into 24 segments in the left arm and 16 segments in the right arm. Eight segments were grouped into one unit and the schematic view of a unit is shown in Fig. 2.16.

Each segment consisted of three SF6W lead-glass blocks and two PMTs. The lead-glass blocks were recycled from the barrel electromagnetic calorimeter of the

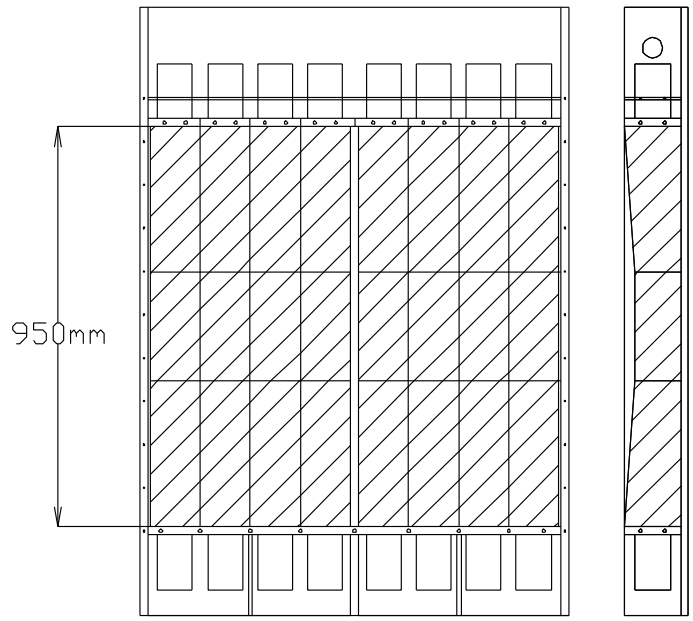

Figure 2.16: Schematic view of a unit of the FLG. The left arm and right arm have three units and two units, respectively. The shaded area represents lead-glass blocks. Taken from Fig. 2.39 in Ref. [74].

TOPAZ experiment at TRISTAN, KEK as the RLG and the SLG. Three lead-glass blocks were stacked vertically and were glued together, resulting in the size of 124 mm in width, and 950 mm in height, and 110 mm in thickness. The central lead-glass block of a stack was re-polished and reshaped into a rectangular shape from an original tapered shape. At the both ends of the lead-glass blocks, the PMT of R1652 of Hamamatsu Photonics, which had a 3-inch diameter photocathode, was installed.

An effective thickness as a Cherenkov radiator was 6.5 radiation length. Cherenkov photons emitted from an electromagnetic shower were propagated into a PMT at the end of a block via the reflections on the surface of the block. The typical energy resolution was $\sigma_E/E \sim 21\%$ for an electron at 1 GeV/c.

2.9 Trigger

2.9.1 Overview

The schematic diagram of the trigger control system is shown in Fig. 2.17. There are two types of trigger logic, one for e^+e^- pairs and the other for K^+K^- pairs. The both types of trigger logic worked simultaneously. The trigger logic for e^+e^- pairs had three levels and that for K^+K^- pairs had two levels.

Signals from the detectors were sent to the first level triggers. If a condition of the either type of trigger logic was satisfied, an event latch was set to busy state. Then, gate signals for an analogue-to-digital converters (ADC) were open and common start (or stop) timing signals for time-to-digital converters (TDC) were sent. At the same time, the higher level triggers were processed. The event latch was kept busy state until a clear signal was produced by the higher level trigger.

If a latched event satisfy all levels of either trigger logic, an accept signal was produced and digitized data in the ADCs and the TDCs was stored in memory modules. After the data transfer to the memory modules was completed, the event latch of busy state was cleared and the trigger control system got ready for the next event again. If a latched event do not satisfy the higher level logic, clear signals were sent to the ADCs, the TDCs and the event latch. The typical duration of busy state was 600 µsec and 50 µsec for a trigger accepted event and a cleared event, respectively.

The data for this analysis was collected in 2001 and 2002. In 2001, the data was collected with both the electron and kaon trigger. In 2002, the data was collected with only the electron trigger logic. In both 2001 and 2002, the second and the third levels of electron trigger logic were switched off, because the event reduction was enough with the first level for electron events.

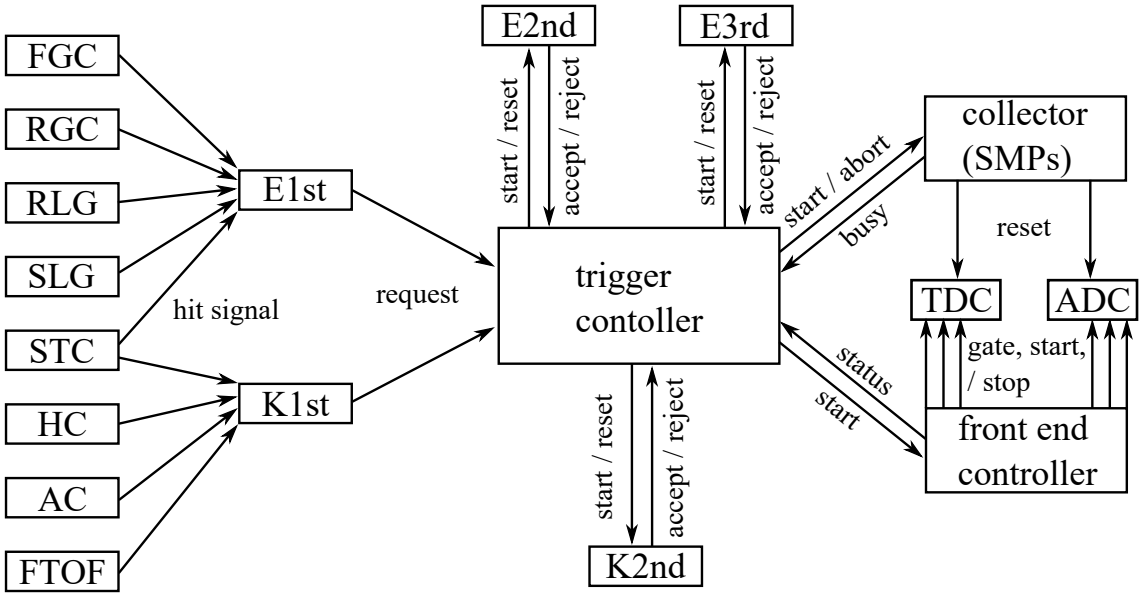

Figure 2.17: Schematic diagram of the trigger control system.

2.9.2 Electron first level trigger logic

The first level electron trigger required the following three criteria to be satisfied:

- One or more hit segments of the FGC in both arms was required to suppress e^+e^- pairs originating from γ conversions and the Dalitz decays. Those events have a small opening angle.
- One or more hit segments of the STC in both arms was required to suppress e^+e^- pairs coming from upstream of the targets such as beam pipes and a Mylar sheet terminating the vacuum of the beam pipe.
- A certain combination of hit segments were required in the FGC and one of the second stage electron identification detectors, RGC, RLG, and SLG. Figure 2.18 shows the allowed combination. The condition effectively selected electrons with momenta greater than 0.4 GeV/c.

A hit signal of each segment was defined as an OR-ed signal of the top and the bottom PMTs with the discriminator threshold of -75 mV, -25 mV, -100 mV, and -480 mV for the FGC, the RGC, the RLG, and the SLG, respectively. This hit signal was also used for the TDC. The most forward segment of the FGC in each arm was excluded from the electron trigger logic to suppress accidental triggers,

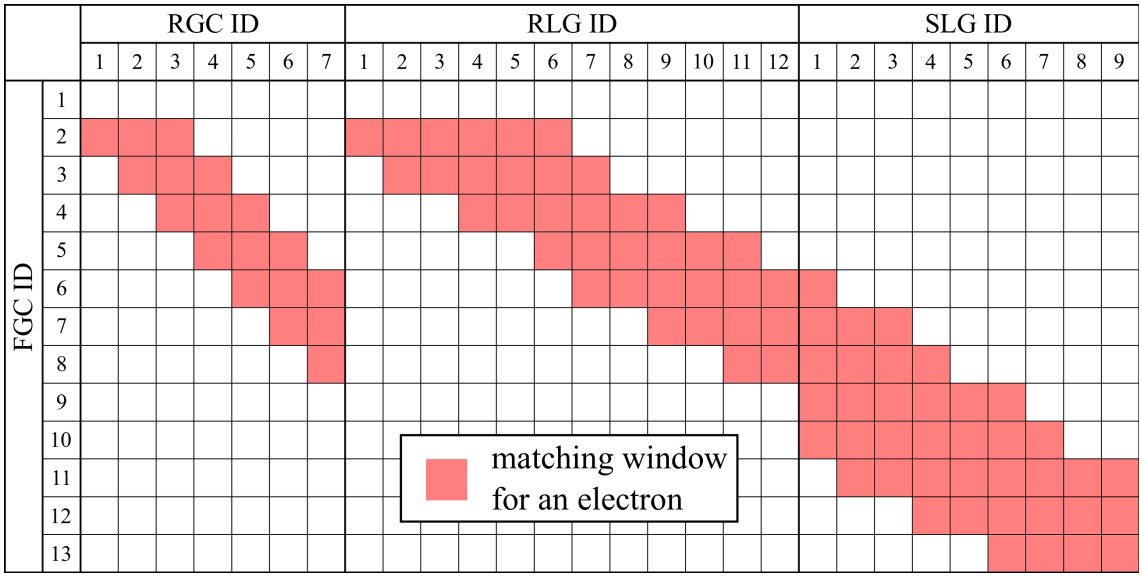

Figure 2.18: Coincidence window between the FGC and the second stage electron identification counters.

because the counting rate was quite high as typically 400 k/spill. All of the first level triggers were based on electric modules of the NIM standard. The decision time was 200–300 ns. A typical trigger request rate of the electron first level trigger was 1.2 k/spill in 2001 and 1.6 k/spill in 2002.

2.10 Data acquisition system

The data-acquisition system (DAQ) consisted of VME [84], TKO [85], and CAMAC [86] based front-end electronics. Schematic diagram of the DAQ is shown in Fig. 2.19. Thirteen TKO crates and one CAMAC crate were controlled via a VME crate. A VME on-board workstation, installed in the VME crate, was the main component in the DAQ. The VME also contains thirteen Super Memory Partner (SMP) modules and a Kinetic K2917 VME-CAMAC interface module. Each SMP worked as a interface module between the VME bus and a TKO bus. A trigger request was provided to all of the SMPs. Then each SMP scans all the channels of ADCs and TDCs in the corresponding TKO crate. The scanned data were stored in the local memories of the SMP. During the scanning, the SMP issued a busy signal to inhibit a further trigger request. This procedure was repeated during spill status was on. At the spill-end, the stored data and the scaler data were read out by the

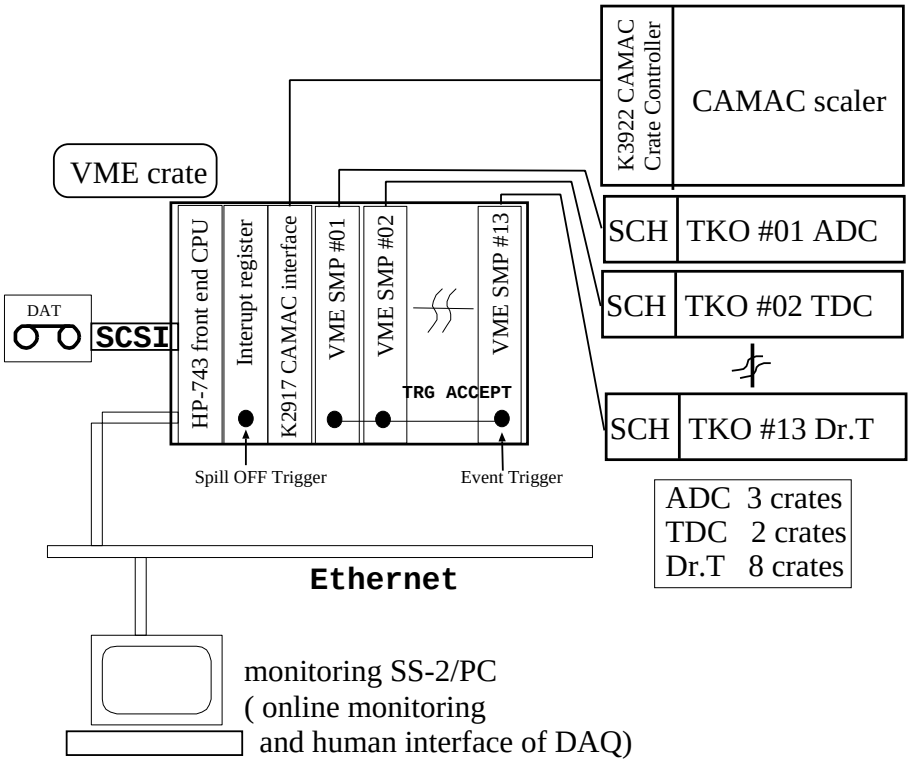

Figure 2.19: Schematic diagram of the DAQ. Taken from Fig. 2.43 in Ref. [74].

VME on-board workstation and were written in a digital data storage tape.

The typical DAQ accept rate was approximately 1k events per spill, corresponding to 3 Mbyte per spill. The live time of the DAQ was 52.1% in 2001 and 58.5% in 2002.

Chapter 3

Analysis

This chapter will be published in a journal within five years and is not open here to the public.

Chapter 4

Results and discussion

This chapter will be published in a journal within five years and is not open here to the public.

Chapter 5

Conclusions

Production of the J/ψ has the attractive feature that it can provide information on both perturbative and nonperturbative aspects of QCD. So far, the production cross section of J/ψ by the hadron interactions had been measured in the wide center of mass energy range, $\sqrt{s} = 6.7$ GeV to 13 TeV. However, no measurements for the J/ψ production at low energy near the production threshold had been carried out yet. Nonperturbative contributions to the J/ψ production are expected to become prominent at lower energies than the former experiments. Intrinsic charm in a nucleon is one of the examples and its existence has not been established. The data of the low energy J/ψ production had been definitely required to investigate the nonperturbative aspect of QCD. The production cross section of the J/ψ at low energy near the production threshold was measured for the first time in the present study.

This thesis was dedicated to the analysis of the production cross section of the J/ψ meson in 12 GeV $p + A$ reactions, corresponding to the center of mass energy $\sqrt{s} = 5.1$ GeV. This is the lowest energy experiment for the J/ψ production by hadron interactions in the all experiments ever conducted. The center of mass energy of the present study is just above the threshold of the simplest final state ppJ/ψ, which is 4.97 GeV.

The production cross section was obtained with the invariant mass spectrum of an e^+e^- pair, which was measured in KEK-PS E325 experiment. The results were $7.0\ ^{+3.4}_{-3.1}$(stat.) $^{+2.9}_{-2.6}$ (syst.) nb for the carbon target and $3.8\ ^{+9.5}_{-3.8}$(stat.) $^{+2.8}_{-3.8}$ (syst.) nb for the copper target. The 95% confidence level upper limits were 21 nb and 33 nb for the carbon target and the copper target, respectively.

The measured cross section for the carbon target showed a slight excess from the contribution of the conventional hard processes calculated with the NRQCD which well reproduced J/ψ production cross sections obtained in former experiments in pp and pA collisions, even considering the possible uncertainty from a PDF and the nuclear effect. This excess was examined in terms of intrinsic charm. The probability

of intrinsic charm $P_{\rm IC}$ was found to be $0.09 \pm 0.06\%$, which was consistent with the results of recent global QCD analyses. This contribution of intrinsic charm to the J/ψ production was also not inconsistent with the J/ψ cross sections obtained in former experiments in pp collisions. The excess due to intrinsic charm was not confirmed in the copper target and the measured cross section was consistent with the contribution of the conventional hard processes calculated with the NRQCD.

The ratio of the cross section for the carbon target to that for the copper target, which represents the mass number dependence, was $1.0\ ^{+2.8}_{-0.7}$ in the present study. This ratio was consistent with the ratio of the contribution of the conventional hard processes. This ratio was also consistent with the ratio of intrinsic charm contribution, even considering the possible absorption of the J/ψ by the nuclear matter.

Due to a large experimental uncertainty, the production cross section of the J/ψ in the present study is consistent with the intrinsic charm scenario and the conventional scenario that the J/ψ production is only originated from hard processes.

Acknowledgements

First, I would like to thank my supervisor, Prof. Kyoichiro Ozawa, who has always been supportive and helpful throughout this time. I have learned from him physics and the attitude toward an experiment. It has been my privilege to be a part of his group, where I have met so many excellent students.

I am grateful to chief scientist Dr. Hideto En'yo of Radiation Lab. in RIKEN Nishina Center, who has gave me the opportunity to work in his laboratory. I have learned the attitude as a scientist from him and it has inspired me. I also thank the staff members of RIKEN Super Combined Cluster system and RIKEN-CCJ, which are PC clusters used for the data analysis.

I express my acknowledgements to all the collaborators of the KEK-PS E325 experiment. In particular, I would like to thank Dr. Satoshi Yokkaichi for his advice and support on this analysis. I would have achieved little without them. I also with to thank Dr. Fuminori Sakuma for useful discussions and encouragements to complete this thesis.

Outside the KEK-PS E325 experiment, I would like to thank Dr. Kazuya Aoki for his kind advice on this thesis. I also learned many experimental techniques from him. I would like to thank Dr. Yuhei Morino for his helpful advice.

This experiment has been fully supported by the staffs of KEK, including the PS beam channel group, the PS floor staff, the on-line group, the electronics division, and the accelerator division.

This work has been partly supported by the Japan Society for the Promotion of Science and a Grant-in-Aid for Scientific Research from the Japan Ministry of Education, Culture, Sports, Science and Technology (MEXT).

Finally, the most thanks go to my family, Kentaro, Mitsuko, Kiyotaka, Chika, and Komachi for the love, steady support, and encouragements. This thesis is dedicated to all five.

Appendices

A Total J/ψ production cross section of former experiments

The total production cross sections of the J/ψ in pA collisions measured in the former experiments are summarized in Table A.1. The data is corrected under the assumption of the mass number dependence A^α with $\alpha = 0.9$ and the symmetric Feynman x_F distributions with respect to $x_F = 0$.

Table A.1: Total production cross section of J/ψ mesons. The data are cited from Ref. [6, 98, 99].

	target	E_{beam} [GeV/c]	$\sqrt{s}$ [GeV]	$\sigma_{J/\psi}$ [nb]
PS [87]	H_2	24	6.8	0.62 ± 0.18
WA39 [88]	H_2	39.5	8.7	2.4 ± 1.2
NA3 [89]	H_2	150	16.8	94 ± 20
NA3 [89]	H_2	200	19.4	122 ± 22
UA6 [90]	H_2	315	24.3	143.6 ± 18.6
ISR [91]	p	—	52	700 ± 320
IHEP [92]	Be	70	11.5	22 ± 6
FNAL [93]	Be	150	16.8	138 ± 46
FNAL [94]	C	225	20.6	180 ± 26
E705 [95]	Li	300	23.8	324 ± 44
FNAL [96]	Be	400	27.4	220 ± 54
E672/E706 [97]	Be	530	31.6	322 ± 70
FNAL [98]	Au	800	38.7	442 ± 88
E771 [99]	Si	800	38.7	390 ± 39

B Effect of the Coulomb potential of target nuclei

The effect of the Coulomb potential of target nuclei on the invariant mass spectrum of $J/\psi \rightarrow e^+e^-$ is evaluated with a Monte-Carlo simulation as follows, and it is found to be negligibly small.

The Coulomb potential $V(r)$ of the target nuclei is written as

$$V(r) = \begin{cases} \dfrac{Ze^2}{2R_{\mathrm{C}}}\left(3 - \left(\dfrac{r}{R_{\mathrm{C}}}\right)^2\right) & r \leq R_{\mathrm{C}} \\ \dfrac{Ze^2}{r} & R_{\mathrm{C}} \leq r, \end{cases}$$

where Z is the atomic number of a target nucleus, e is the elementary charge, R_{C} is the radius of a target nucleus, and r is the radial distance from the center of a target nucleus. The radius of the carbon target and the copper target is 2.47 fm and 3.88 fm [100], respectively. The J/ψ mesons are uniformly produced in a nucleus. The kinematics of the J/ψ mesons is evaluated as described in Sec. 3.8.2. The produced J/ψ mesons move inside a nucleus without any interaction and decay into an e^+e^- pair according to its natural total width. In the simulation, both tracks, e^+ and e^-, are tracked under the Coulomb potential of a target nucleus until they are 10 nm away from the target nucleus. The difference of the invariant mass of an e^+e^- pair between with and without the Coulomb potential is shown in Fig. B.1. The mass difference is less than 0.1 keV/c^2 for both targets, which is negligibly small.

C Transverse momentum distribution of J/ψ mesons

The transverse momentum distributions of J/ψ mesons in three rapidity regions, $1 < y < 4/3$, $4/3 < y < 5/3$, and $5/3 < y < 2$, after the correction of the electron identification and the acceptance are shown in Fig. C.1 and C.2. Figure C.2 is divided into three bins while Fig. C.1 is divided into two bins.

D Area density of targets

The weight, the length of four sides, and the diagonal length of each square shaped target were measured to estimate the area density of that target. The area density of each target n_{target} is written as

$$n_{\mathrm{target}} = \frac{WN_A}{AS}, \tag{5.1}$$

where W denotes the target weight, N_A denotes the Avogadro constant of 6.02214×10^{23} [101], A denotes the atomic weight, and S denotes the area of the target. The

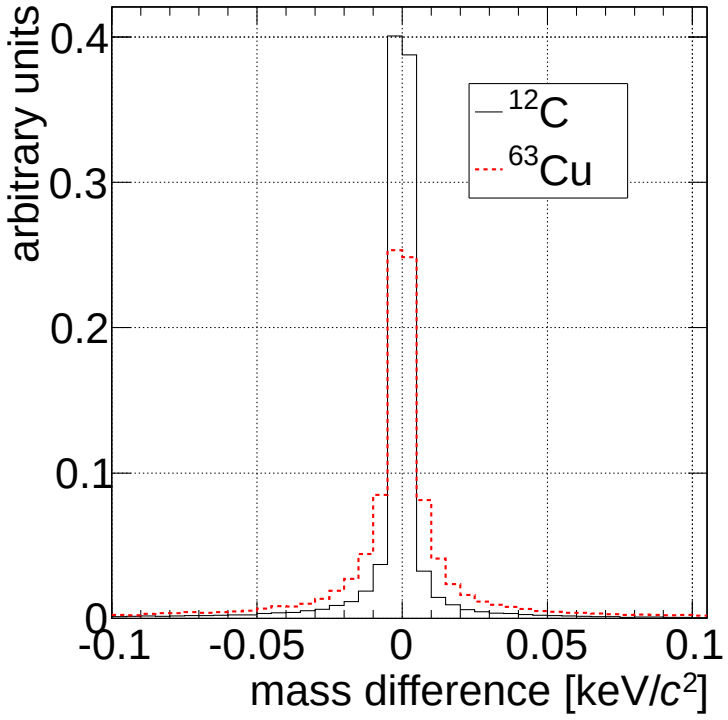

Figure B.1: Difference of the invariant mass of $J/\psi \rightarrow e^+e^-$ between with and without the Coulomb potential of target nuclei.

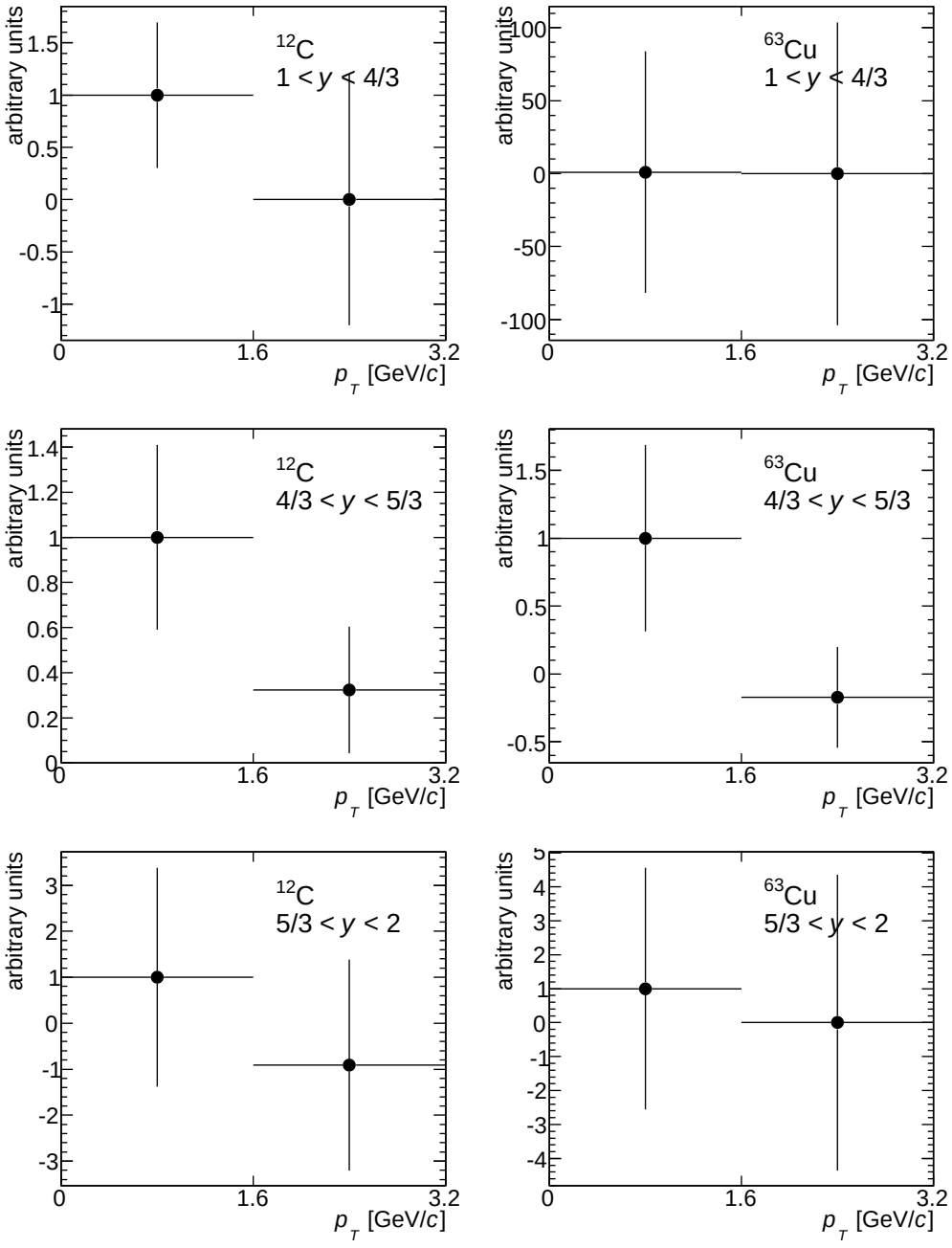

Figure C.1: Transverse momentum distributions of J/ψ mesons in three rapidity regions after the correction of the electron identification efficiency and the acceptance.

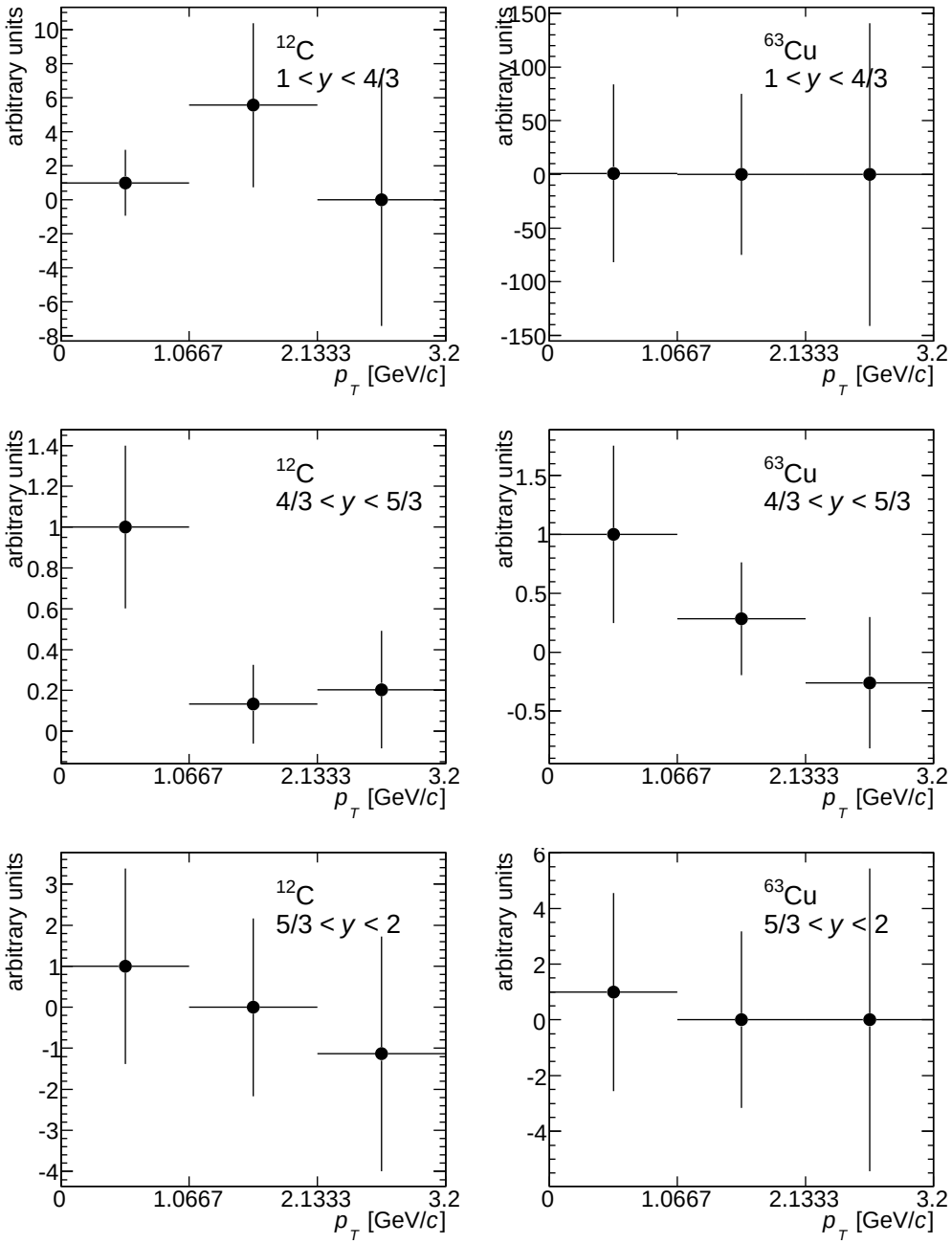

Figure C.2: Transverse momentum distributions of J/ψ mesons in three rapidity regions after the correction of the electron identification efficiency and the acceptance. The x-axis is divided into three bins.

atomic weight of the carbon target and the copper target are 12.011 and 63.546 [77], respectively. With Heron's formula, The area of each target is expressed as

$$\begin{aligned} S &= \sqrt{a(a-L_1)(a-L_2)(a-L_5)} \\ &\quad + \sqrt{b(b-L_3)(b-L_4)(b-L_5)}, \\ a &= (L_1+L_2+L_5)/2, \text{ and} \\ b &= (L_3+L_4+L_5)/2, \end{aligned}$$

where L_1, L_2, L_3, and L_4 represent the four side of a target and L_5 is the diagonal length. The weight was measured with an accuracy of 0.00001 g and the length was measured with an accuracy of 0.05 mm. Measurements of the weight and the size were performed by the supplying company. Measured values and calculated values for targets used in 2001 and used in 2002 are summarized in Table D.1 and D.2, respectively.

Table D.1: Size and the weight of the targets in 2001.

	C	Cu (total)	Cu1	Cu2
W [g]	2.30230	0.91643	0.45663	0.45980
L_1 [mm]	50.00	—	25.00	25.30
L_2 [mm]	50.05	—	25.05	25.05
L_3 [mm]	50.00	—	25.25	25.25
L_4 [mm]	50.05	—	25.00	25.25
L_5 [mm]	70.70	—	35.25	35.50
S [mm^2]	2502.5 ± 3.5	1264.3 ± 2.5	628.7 ± 1.8	635.6 ± 1.8
$n_{\text{target}} \times 10^{-25}$ [m^{-2}]	4.6128 ± 0.0065	1.3738 ± 0.0027	0.6883 ± 0.0019	0.6855 ± 0.0019

Table D.2: Size and the weight of the targets in 2002.

	C	Cu (total)
W [g]	4.60658	7.1594
L_1 [mm]	50.05	—
L_2 [mm]	50.00	—
L_3 [mm]	50.05	—
L_4 [mm]	50.05	—
L_5 [mm]	70.65	—
S [mm^2]	2503.7 ± 3.5	985.0 ±2.7
$n_{\mathrm{target}} \times 10^{-25}$ [m^{-2}]	9.225 ± 0.013	2.7552 ± 0.0074

	Cu1	Cu2	Cu3	Cu4
W [g]	0.17911	0.17920	0.17841	0.17922
L_1 [mm]	9.80	9.85	9.80	9.80
L_2 [mm]	25.10	24.80	25.25	25.00
L_3 [mm]	9.90	9.90	9.80	9.80
L_4 [mm]	24.90	25.10	24.80	25.00
L_5 [mm]	27.00	26.60	26.60	26.75
S [mm^2]	246.2 ± 1.4	246.3 ± 1.3	246.3 ± 1.3	246.2 ± 1.3
$n_{\mathrm{target}} \times 10^{-25}$ [m^{-2}]	0.6894 ± 0.0038	0.6895 ± 0.0037	0.6844 ± 0.0037	0.6897 ± 0.0037

Bibliography

[1] J.J Aubert *et al.*, Phys. Rev. Lett. **33**, 1404 (1974).

[2] J.E Augustin *et al.*, Phys. Rev. Lett. **33**, 1406 (1974).

[3] C. McNeile *et al.* (HPQCD Collaboration), Phys. Rev D **82**, 034512 (2010).

[4] C. Patrignani *et al.* (Particle Data Group 2016), Chin. Phys. C **40**, 100001 (2016).

[5] M. Beneke and I.Z. Rothstein, Phys. Rev. D **54**, 2005 (1996).

[6] G. A. Schuler, CERN-TH.7170/94

[7] C.N. Yang, Phys. Rev. **77**, 242 (1950)

[8] D. Binosi and L. Theußl, Comp. Phys. Commun. **161**, 76 (2004).

[9] M. Cacciari *et al.*, Phys. Lett. B **356**, 553 (1995).

[10] J.P. Lansberg, Phys. Lett. B **695**, 149 (2011)

[11] H. Fritzsch, Phys. Lett. B **67**, 217 (1977).

[12] F. Halzen, Phys. Lett. B **69**, 105 (1977).

[13] M. Glück, J.F. Owens, and E. Reya, Phys. Rev. D **17**, 2324 (1978).

[14] V. Barger, W.Y. Keung, and R.J.N. Phillip, Phys. Lett. B **91**, 253 (1980).

[15] J.F. Amundson, O.J.P. Éboli, E.M. Gregores, F. Halzen, Phys. Lett. B **390**, 323 (1997).

[16] W.E. Caswell and G.P. Lepage, Phys. Lett. B **167**, 437 (1986).

[17] B.A. Thacker and G.P. Lepage, Phys. Rev. D **43**, 196 (1991).

[18] G.T. Bodwin, E. Braaten, and G.P. Lepage, Phys. Rev. D **51**, 1125 (1995).

[19] G. Altarelli and G. Parisi, Nucl. Phys. B **126**, 298 (1977).

[20] Yu. L. Dokshitser, Sov. Phys. JETP **46**, 641 (1977).

[21] V.N. Gribov and L.N. Lipatov, Sov. J. Nucl. Phys. **15**, 438 (1972).

[22] D. Stump *et al.*, JHEP10(2003)046.

[23] S. Catani *et al.*, Phys. Rev. Lett. **93**, 152003 (2004).

[24] J. Pumplin *et al.*, JHEP07(2002)012.

[25] J.J. Aubert *et al.* (The European Muon Collaboration), Phys. Lett. B **123**, 275 (1983).

[26] N. Armesto, J. Phys. G: Nucl. Part. Phys. **32**, R367 (2006).

[27] M. Arneodo, Phys. Rep. **240**, 301 (1994).

[28] D. F. Geesaman *et al.*, Ann. Rev. Nucl. Part. Sci. **45**, 337 (1995).

[29] K.J. Eskola, H. Paukkunen, and C.A. Salgado, JHEP04(2009)065.

[30] C. Lourenço *et al.*, JHEP02(2009)014.

[31] S.J. Brodsky, P. Hoyer, C. Peterson, and N. Sakai, Phys. Lett. B **93**, 451 (1980).

[32] J.J. Aubert *et al.* (The European Muon Collaboration), Nucl. Phys. B **213**, 31 (1983).

[33] J. Pumplin *et al.*, Phys. Rev. D **75**, 054029 (2007)

[34] R. Vogt and S.J. Brodsky, Phys. Lett. B **349**, 569 (1995).

[35] R. Vogt, Phys. Rev. C **61**, 035203 (2000).

[36] S.J. Brodsky and P. Hoyer, Phys. Rev. Lett. **63**, 1566 (1989).

[37] F.S Navarra *et al.*, Phys. Rev. D **54**, 842 (1996).

[38] W. Melnitchouk and A.W. Thomas, Phys. Lett. B **414**, 134 (1997).

[39] T.J. Hobbs *et al.*, Phys. Rev. D **89**, 074008 (2014).

[40] F.S. Navarra and M. Nielsen, Phys. Lett. B **443**, 285 (1998).

[41] H. Abramowicz *et al.* (The H1 and ZEUS Collaborations), Eur. Phys. J. C **73**, 2311 (2013).

[42] E. Hoffmann and R. Moore, Z. Phys. C **20**, 71 (1983).

[43] B.W. Harris, J. Smith, and R. Vogt, Nucl. Phys. B **461**, 181 (1996).

[44] F.M. Steffens, W. Melnitchouk, and A.W. Thomas, Eur. Phys. J. C **11**, 673 (1999).

[45] A.D. Martin *et al.*, Eur. Phys. J. C **63**, 189 (2009).

[46] P. Jimenez-Delgado *et al.*, Phys. Rev. Lett. **114**, 082002 (2015).

[47] S. Duan, C.S. An, and B. Saghai, Phys. Rev. D **93**, 114006 (2016),

[48] M.G. Albrow *et al.*, Nucl. Phys. B **108**, 1 (1976).

[49] D. Drijard *et al.*, Phys. Lett B **81**, 250 (1979).

[50] K.L. Giboni *et al.*, Phys. Lett B **85**, 437 (1979).

[51] W. Lockman *et al.*, Phys. Lett B **85**, 443 (1979).

[52] D. Drijard *et al.*, Phys. Lett B **85**, 452 (1979).

[53] M. Glück, E. Hoffmann, and E. Reya, Z. Phys. C **13**, 119 (1982).

[54] M. Glück, E. Reya, and A. Vogt, Eur. Phys. J. C **5**, 461 (1998).

[55] A.D. Martin *et al.*, Eur. Phys. J. C **4**, 463 (1998)

[56] W.K. Tung *et al.*, JHEP02(2007)053

[57] P. Jimenez-Delgado and E. Reya *et al.*, Phys. Rev. D **89**, 074049 (2014).

[58] D. de Florian and R. Sassot, Phys. Rev. D **69**, 074028 (2004).

[59] C.S. An and B. Saghai, Phys. Rev. C **85**, 055203 (2012).

[60] M.J. Leitch *et al.* (FNAL E866/NuSea Collaboration), Phys. Rev. Lett. **84**, 3256 (2000).

[61] R. Arnaldi *et al.*, Phys. Lett. B **706**, 263 (2012).

[62] D.M. Alde *et al.*, Phys. Rev. Lett. **66**, 133 (1991).

[63] J. Badier *et al.* (NA3 Collaboration), Z. Phys. C **20**, 101 (1983).

[64] P. Hoyer *et al.*, Phys. Lett. B **246**, 217 (1990).

[65] M.A. Vasiliev *et al.* (FNAL E866/NuSea Collaboration), Phys. Rev. Lett **83**, 2304 (1999).

[66] D.M. Alde *et al.*, Phys. Rev. Lett **64**, 2479 (1990).

[67] M. Naruki *et al.*, Phys. Rev. Lett. **96**, 092301 (2006).

[68] R. muto *et al.* (KEK-PS E325 Collaboration), Phys. Rev. Lett. **98**, 042501 (2007).

[69] F. Sakuma *et al.* (KEK-PS E325 Collaboration), Phys. Rev. Lett. **98**, 152302 (2007).

[70] M. Takasaki *et al*, KEK Internal 95-1, (1995), https://lib-extopc.kek.jp/preprints/PDF/1995/9526/9526001.pdf.

[71] M. Sekimoto *el al.*, Nucl. Instr. and Meth. A **516**, 390 (2004).

[72] I. Adachi *et al.*, Nucl. Instr. and Meth. A **355**, 390 (1995).

[73] M. Ishino *et al.*, Nucl. Instr. and Meth. A **457**, 581 (2001).

[74] F. Sakuma, PhD thesis, Department of Physics, Faculty of Science, Kyoto University (2007).

[75] Y. Sugaya, Nucl. Instr. and Meth. A **368**, 635 (1996).

[76] TOSCA/OPERA-3d Software. Vector Fields Ltd., Oxford, U. K..

[77] J. Meija *et al.* (IUPAC Technical Report), Pure Appl. Chem. **88(3)**, 265 (2016).

[78] O. Sasaki *et al.* (ATLAS TGC Collaboration), ATLAS TGC ASD IC (1999), http://atlas.kek.jp/tgcelec/ASD/ASD-PRR.pdf.

[79] R. Veenhof, Garfield - simulation of gaseous detectors, https://cern.ch/garfield.

[80] S. Agostinelli *et al.*, Nucl. Instr. and Meth. A **506**, 250 (2003).

[81] R. Muto, PhD thesis, Department of Physics, Faculty of Science, Kyoto University (2007).

[82] H. Hinterberger and R. Winston, Rev. Sci. Instr. **37**, 1094 (1966).

[83] S. Kawabata *et al.*, Nucl. Instr. and Meth. A **270**, 11 (1988).

[84] IEEE Standard for a Versatile Backplane Bus: VMEbus, ANSI/IEEE Std 1014–1987 (1987),
ANSI/IEEE Std, 1014–1987.

[85] T.K. Ohska *et al.* (KEK Data Acquisition Development Working Group), KEK Report 85-10 (1985),
http://www.iaea.org/inis/collection/NCLCollectionStore/_Public/18/009/18009738.pdf.

[86] I.F. Kolpakov, Comp. Phys. Commun. **15**, 341 (1978).

[87] A. Bamberger *et al.*, Nucl. Phys. B **134**, 1 (1978)

[88] M.J. Corden *et al.*, Phys. Lett. B **98**, 220 (1981)

[89] J. Badier *et al.*, Z. Phys. C **20**, 101 (1983)

[90] C. Morel *et al.*, Phys. Lett. B **252**, 505 (1990)

[91] E. Nagy *et al.*, Phys. Lett. B **60**, 96 (1975)

[92] Yu.M. Antipov *et al.*, Phys. Lett. B **60**, 309 (1976)

[93] K.J. Anderson *et al.*, Phys. Rev. Lett. **37**, 799 (1976)

[94] J.G. Branson *et al.*, Phys. Rev. Lett. **38**, 1331 (1977)

[95] L. Antoniazzi *et al.*, Phys. Rev. Lett. **70**, 383 (1993)

[96] H.D. Snyder *et al.*, Phys. Rev. Lett. **36**, 1415 (1976)

[97] V. Abramov *et al.*, Fermilab Pub 91/62E (1991)

[98] M.H. Schub *et al.*, Phys. Rev. D **52**, 1307 (1996)

[99] T. Alexopoulos *et al.*, Phys. Lett. B **374**, 271 (1996)

[100] I. Angeli and K.P. Marinova, Atom. Data and Nucl. Data **99**, 69 (2013).

[101] P.J. Mohr *et al.*, Rev. Mod. Phys. **88**, 035009 (2016).